Available online at www.sciencedirect.com
ScienceDirect
Progress in Materials Science 51 (2006) 983–1031
Progress in Materials Science
www.elsevier.com/locate/pmatsci

Low-dimensional SiC nanostructures: Fabrication, luminescence, and electrical properties

J.Y. Fan [a,b], X.L. Wu [a,b,*], Paul K. Chu [b,*]

[a] *National Laboratory of Solid State Microstructures & Department of Physics, Nanjing University, Nanjing 210093, China*
[b] *Department of Physics and Materials Science, City University of Hong Kong, Tat Chee Avenue, Kowloon, Hong Kong, China*

Received 5 December 2005; received in revised form 2 January 2006; accepted 11 January 2006

Abstract

Nanostructured silicon carbide has unique properties that make it useful in microelectronics, optoelectronics, and biomedical engineering. In this paper, the fabrication methods as well as optical and electrical characteristics of silicon carbide nanocrystals, nanowires, nanotubes, and nanosized films are reviewed. Silicon carbide nanocrystals are generally produced using two techniques, electrochemical etching of bulk materials to form porous SiC or embedding SiC crystallites in a matrix such as Si. Luminescence from SiC crystallites prepared by these two methods is generally believed to stem from surface or defect states. Stable colloidal 3C-SiC nanocrystals which exhibit intense visible photoluminescence arising from the quantum confinement effects have recently be produced. The field electron emission and photoluminescence characteristics of silicon carbide nanostructures as well as theoretical studies of the structural and electronic properties of the materials are described.

PACS: 81.07.−b; 61.46.+w; 73.22.−f; 78.67.−n; 78.66.−w; 79.70.+q

Contents

* Corresponding authors. Address: Department of Physics and Materials Science, City University of Hong Kong, Tat Chee Avenue, Kowloon, Hong Kong, China.
E-mail addresses: hkxlwu@nju.edu.cn (X.L. Wu), paul.chu@cityu.edu.hk (P.K. Chu).

0079-6425/$ - see front matter
doi:10.1016/j.pmatsci.2006.02.001

1. Introduction

Silicon carbide nanostructures have very unique properties which bode well for applications in microelectronics and optoelectronics and have thus attracted much interest from the materials and device communities. In the microelectronics industry, silicon carbide is regarded as a promising substitute for silicon, especially in high power, high temperature, and high frequency devices [1,2]. Recent advances in the preparation of ultra-high quality SiC single-crystals have in fact paved the way for wider uses of silicon carbide in microelectronic devices [3].

Among the different kinds of SiC nanostructures, SiC nanocrystals which have potential applications as nanoscale light emitters were the first to receive attention and have been studied extensively in the last ten years. Optically, bulk SiC shows weak emission at room temperature on account of its indirect band gap [4]. However, the emission intensity can be significantly enhanced when the crystallite size diminishes to several or tens of nanometers [5,6]. This is thought to be caused by depressed non-radiative recombination in the confined clusters [7]. In accordance with the quantum confinement (QC) effect, photoluminescence (PL) of the crystallites with diameters below the Bohr radius of bulk excitons is shifted to blue with decreasing sizes [8,9]. Consequently, wavelength-tunable emissions can be achieved by preparing crystallites with different sizes. The large band gap of SiC (2.23 eV for 3C-SiC) renders the nanocrystals a good candidate as blue and ultraviolet (UV) light emitters in displays. This is in contrast to silicon crystallites from which strong and stable emissions in these spectral ranges are difficult to achieve [6]. Moreover, the high chemical and thermal stabilities [10] of silicon carbide make the luminescence from these nanocrystals very stable enabling the use of the materials in harsh environments and demanding

applications. Combined with their excellent biocompatibility, especially blood compatibility, low density, and high rigidity [11,12], SiC nanocrystals are potentially useful in biology and medicine as well, for example, in bio-labeling [13,14].

Luminescence from SiC crystallites has been experimentally studied [15–19] and there are several methods to fabricate luminescent SiC crystallites. The older method is based on electrochemical etching of bulk SiC [20,21], mostly the 3C or 6H polytypes [15–18]. Since the mid-1990s, several groups have attempted to attain blue emission from SiC nanocrystals produced by new techniques such as C ion implantation into bulk Si followed by etching [19], co-implantation of C and Si into SiO_2 [22], C_{60} introduction into porous silicon followed by annealing [23], and so on. However, the luminescent properties of SiC nanocrystals have been observed to be quite variable and strongly depend on the fabrication methods and even on the specific measurements. The emission band can span a wide spectral range from 400 to 500 nm. No luminescence exhibiting obvious quantum confinement has been reported until recently. This is in contrast to porous Si [5,24] and Si nanocrystals [25–28] from which quantum confinement can be more easily observed. As a binary compound, silicon carbide has complex surface states and structures [29–32]. The main reasons why quantum confinement is not easily achieved in SiC are that there are many surface or defect states which dominate the luminescence and that the SiC nanocrystals are too large [17]. Recently, colloidal 3C-SiC nanocrystals with diameters ranging from 1 to 8 nm have been fabricated via electrochemical etching of polycrystalline 3C-SiC wafers followed by ultrasonic treatment [33]. They yield intense visible PL in a large wavelength range as predicted by the quantum confinement effect [34]. These 3C-SiC nanocrystals that exhibit wavelength-tunable and strong luminescence have potential applications in nano-optoelectronics and biology/medicine [35]. As an extension of this technique, SiC/polymer composite films emitting blue light have also been synthesized successfully [36].

On the theoretical front, the structure and electronic properties of SiC nanostructures have been investigated employing semi-empirical and first-principle calculations [34,37,38]. The results suggest that the band gap of SiC nanostructures has a strong dependence on their sizes and surface compositions.

Recently, one-dimensional (1D) SiC nanostructures such as nanowires [39], nanotubes [40], and so on have attracted a lot of interest because they play a crucial role as the building blocks in molecular electronics [41]. Silicon carbide nanowires that have outstanding mechanical property and high electrical conductance can be used to reinforce composite materials or as nanocontacts in a harsh environment. Moreover, the materials have good field electron emission properties and biocompatibility. In the paper, we review the various techniques used to synthesize 1D SiC nanostructures. The electrical and optical properties of these nanostructures are also discussed. In comparison with zero or one-dimensional nanostructures, not much is known about the fabrication and luminescent properties of nanocrystalline SiC films [42], and so this research area will only be briefly reviewed here.

2. Fabrication of and luminescence from porous SiC

2.1. Electrochemical etching of bulk SiC

Canham [5] first demonstrated that luminescent Si nanocrystallites could be fabricated by electrochemical etching of bulk Si. The resulting porous structure is composed of interconnected nanoparticles or nanowires with sizes ranging from less than one nanometer to

tens of nanometers, depending on the fabrication conditions. Similarly, porous SiC can be prepared in this way. Etching can be used to selectively pattern bulk SiC for microelectronics and produce luminescent porous SiC for optoelectronics. However, one technical challenge remains. Unlike Si, there are no chemical etchants that attack SiC at room temperature, with the exception of phosphoric acid which only causes slow decomposition [43]. One effective etching technique for β-SiC is reactive ion etching (RIE) with etching rates between 50 and 200 nm/min [44]. Anodic etching of diffraction gratings made of n-type β- and α-SiC has been conducted in the presence of light illumination [45]. Laser-assisted photo-electro-chemical etching of n-type β-SiC using an electrolyte comprising H_2O, HF, and H_2O_2 in the ratios of 205:5:1 has been proposed [20], and etching rates of 1–100 μm/min that are higher than those reported using other etching methods have been achieved. The frequency-doubled 257 nm line from an Ar^+ laser generates holes near the surface. These holes are transported in the presence of an external bias to the SiC/solution interface where dissolution occurs via anodic oxidation of SiC and removal of the oxide by HF. The presence of water is necessary here. After etching, the surface layer which is carbon rich (Si/C = 0.22) extends 0.5 nm into the bulk materials. This carbon-rich layer is formed by unoxidized carbon on the sample surface or Si depletion due to the dissolution of the native SiO_2 layer on the SiC surface. In order to further oxidize the unoxidized carbon, a small amount of H_2O_2 (0.5%) can be added to the solution from which CO_2 bubbles are formed.

Based on this method, a patterning technique has been proposed for n-type SiC epilayers on p-type substrates serving as an etch stop [46]. The surface band bending of n- and p-type SiC is different thereby affecting the charge transport across the semiconductor/liquid junction. As a result, etching of p-type semiconductors occurs at much higher potentials than in n-type materials. Hence, by selecting an appropriate potential, the n-type materials can be photo-electro-chemically etched while the p-type substrate can act as an etch stop. In fact, it has been found that 6H-SiC can be etched rapidly using this technique.

Bulk SiC can be electrochemically etched to form porous SiC [47,21]. Fig. 1 shows a plan view TEM micrograph of the porous 6H-SiC layer prepared by electrochemical

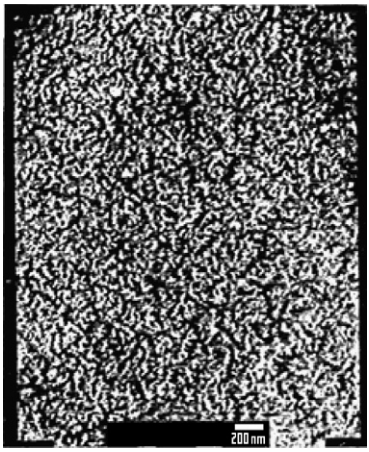

Fig. 1. Plan view TEM micrograph of an anodized n-type 6H-SiC sample. Anodization is conducted at $V = 1.4\ V_{sce}$ and $I \approx 300\ mW/cm^2$ in 2.5% HF. The horizontal bar indicates 200 nm [47].

etching of single-crystal n-type 6H-SiC under UV illumination [47]. The bright areas represent pores and there exist central pores from which smaller pores branch out. These structures resemble the dendritic structures observed in metals and are similar to the morphology observed in porous Si [48]. Recently, fracturing of a hydrogen-rich surface has been shown to yield a porous layer of silicon nanocrystals [49]. By means of a fractal model, the evolution of the nanocrystallites' fractal dimension (2.1–2.4) as a function of the porosity is deduced by correlating the modeled results to empirically determined hydrogen concentrations. This is similar to that of SiC. As shown in Fig. 1, the pore sizes vary between 10 and 30 nm and the spacing between the central pores is less than 150 nm, while adjacent branches appear to be separated by several nanometers. The pore morphology varies across the surface of the porous SiC sample. This can be attributed to the nonuniformity in the photo-electro-chemical process as a result of the change of the UV intensity or localized electrode potential. Selected area diffraction (SAD) indicates that the anodized porous layer is composed of single-crystal 6H-SiC, demonstrating that the dot- or wire-like structures are well connected to the substrate. With regard to the optical properties, only very weak UV luminescence has been observed and its origin is still unknown.

The formation mechanism of the porous structures in Si is complicated and consensus on the formation mechanism has not been reached [48]. One puzzling question is the unusually high stability of the thin Si fibers against electrolytic attack. Similarly, it is not clear how the porous structure forms in SiC. It has been suggested that the large amount of defects found in sublimation-grown 6H-SiC may initiate these pores. Another possibility is that pores may begin to form due to variations in the surface chemistry.

Porous boron-doped p-type and undoped β-SiC samples can be produced by electrochemical anodization [21]. TEM data indicate that both the doped and undoped samples possess porous structures similar to porous Si. However, there are some differences between the two types of samples. The boron-doped sample shows a wire-like porous structure with diameters ranging from 50 to 70 nm. On the other hand, the undoped porous sample has an irregular structure with a much smaller size. The thickness of the porous layer in both samples is about 0.5 μm. The chemical reaction leading to anodic dissolution of β-SiC is believed to be as follows:

$$\mathrm{SiC} + 8\mathrm{OH}^- + \lambda \mathrm{e}^+ \rightarrow \mathrm{SiO_2} + \mathrm{CO_2} + 4\mathrm{H_2O} + (8-\lambda)\mathrm{e}^- \quad \text{and} \tag{1}$$

$$\mathrm{SiO_2} + 6\mathrm{HF} \rightarrow \mathrm{H_2SiF_6} + 2\mathrm{H_2O} \tag{2}$$

where λ is smaller than 8, and e^+ and e^- represent a hole or an electron, respectively. No visible photoluminescence is observed from either the undoped or boron-doped porous β-SiC sample at room temperature. The crystallite diameter is about 20 nm and is too large to exhibit quantum confinement [50].

It is well known that when a porous layer forms on Si, the sample changes from being semiconducting to insulating. The electrical properties and formation mechanism of porous silicon carbide have been studied [51]. The porous SiC is prepared by electrochemical etching of n-type 6H-SiC single crystals doped with $1–3 \times 10^{18}\,\mathrm{cm}^{-3}$ nitrogen in 2.5 M NH_4F and HF solutions with or without UV light illumination. The SEM images in Fig. 2 disclose considerable differences between these two kinds of samples. The average fiber thickness is about 0.5–1 μm in the dark-etched material whereas it is below 50 nm in the photo-assisted etched materials. The results are consistent with those in others

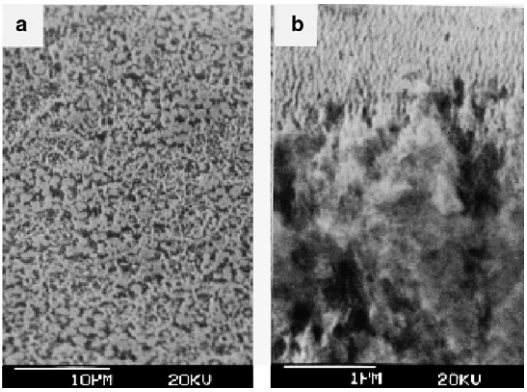

Fig. 2. SEM images of porous SiC: (a) dark-etched materials, plan view; (b) photo-assisted etched materials, trench wall [51].

reports [47,21] and show that the sample preparation conditions affect the structure of the materials. A correlation between the fiber size and resistivity of the porous SiC is observed. A smaller fiber size results in a semi-insulating material due to Fermi-level pinning to the surface states, and a model has been proposed to explain the self-regulation of the fiber size in the porous SiC formation. The model relates the blocking of the fiber dissolution process to the increase of resistivity in a thin wire due to Fermi-level pinning.

Based on further studies on the photo-electro-chemical etching of n- and p-type silicon carbide, several models have been proposed to explain the formation of the porous structure [52,53]. Photo-electro-chemical etching of highly-doped n-type 4H-SiC along different crystallographic orientations has been carried out in diluted hydrofluoric acid under low voltage and/or low current conditions [52]. The SEM pictures show that anodization of hexagonal 4H-SiC proceeds anisotropically and leads to pore formation. It is proposed that under UV illumination, the crystallographic planes terminated with silicon atoms are more resistant to electrolytic attack than those terminated with carbon. As illustrated in Fig. 3, this model is used to explain the observed triangular-channel pore morphology and that the resulting pore structure does not depend on the direction of the external electric field applied to the sample.

In p-type 6H-SiC, pore formation is favored on the C-terminated face while complete dissolution occurs on the Si-terminated face [53]. When the C-terminated face is etched, the thickness of the pore wall diminishes with increasing current density. The surface morphology of the porous structure depends on the polishing conditions prior to anodization while the bulk porous structure is independent of the surface treatment (Fig. 4). The overall reactions are suggested to be as follows:

$$\mathrm{SiC} + \mathrm{H_2O} + 6\mathrm{F^-} + 6\mathrm{h^+} = \mathrm{SiF_6^{2-}} + \mathrm{CO} + 2\mathrm{H^+} \tag{3}$$

$$\mathrm{SiC} + 2\mathrm{H_2O} + 6\mathrm{F^-} + 8\mathrm{h^+} = \mathrm{SiF_6^{2-}} + \mathrm{CO_2} + 4\mathrm{H^+} \tag{4}$$

Well-organized columnar structures have been observed to form in alumina [54] and silicon [55]. Similar self-organized structures have also been seen in porous 6H-SiC [56]. Under certain conditions, channels are found to propagate nearly parallel to the *c* axis. The pores in 6H-SiC tend to propagate initially nearly parallel to the base plane and gradually change direction to align with the *c* axis.

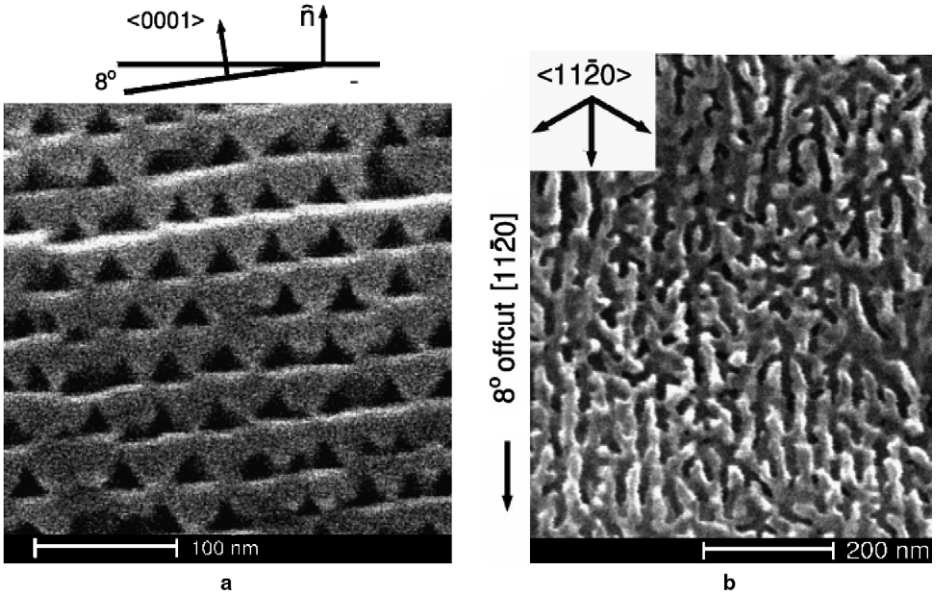

Fig. 3. (a) Cross-sectional SEM image of a vicinal ⟨0 0 0 1⟩ n-type 4H-SiC sample photo-electro-chemically etched at 3 V in aqueous HF. Perforating triangular pores are arranged in layers about 35 nm thick. (b) Plan view SEM image of a 4H-SiC sample, 8° off the *c* axis towards ⟨1 1 2 0⟩, anodized to obtain the triangular porous morphology [52].

So far, we have described methods utilizing electrochemical anodization in HF solutions. Several other methods have also been reported [57,58]. An electroless method that produces porous 6H-SiC without requiring electrical contact during etching is quite effective [57]. The platinum metal deposited on the wafer before etching acts as a catalyst to reduce chemical oxidation. UV illumination injects holes into the valence band, and the holes subsequently participate in the oxidation and dissolution of the substrate. HF and $K_2S_2O_8$ aqueous solutions are used as the etchants. It is hypothesized that SiC is oxidized in an $8e^-$ process in which the products react with HF to produce a soluble product according to the following equations:

Cathode (Pt):

$$4S_2O_8^{2-} + h\nu \rightarrow 8SO_4^{2-} + 8h^+ \tag{5}$$

Anodic (SiC):

$$SiC + 4H_2O + 8h^+ \rightarrow SiO_2 + 8H^+ + CO_2 \tag{6}$$

$$SiO_2 + 6HF \rightarrow H_2SiF_6 + 2H_2O \tag{7}$$

Using either a concentrated or diluted HF solution, an etching time of less than 30 min yields a ridged porous structure [Fig. 5(a)]. Generally, the porous morphology is homogeneous across the wafer surface, although occasional pockets with varying degrees of porosity have been detected. A longer etching time produces different morphologies that depend on the etching solutions. In the case of diluted HF, a sponge-like morphology is observed [Fig. 5(b)]. The etched samples display similar PL characteristics with respect to the unetched wafer but with slightly enhanced intensity and shifted emission wavelength.

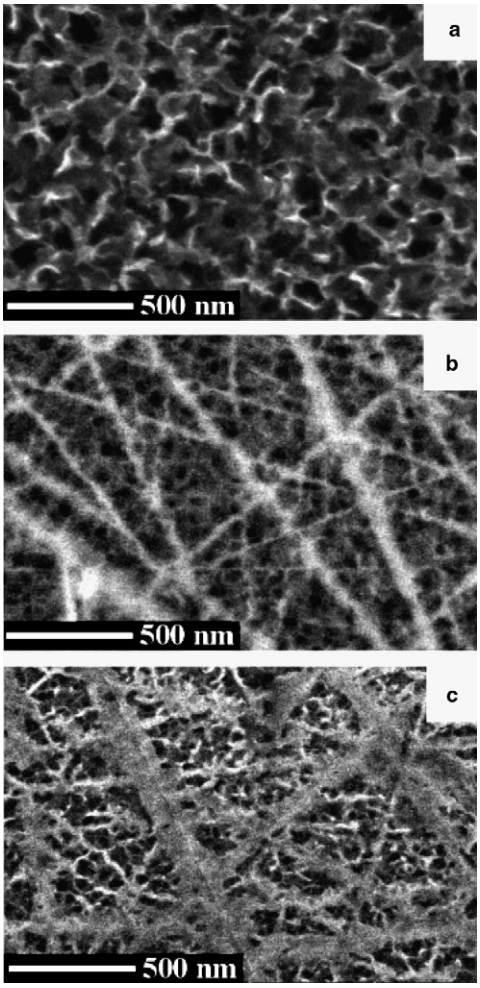

Fig. 4. Plan view SEM images of porous p-type ($p \sim 2.0 \times 10^{18}$ cm^{-3}) C-face 6H-SiC samples treated prior to electrochemical etching by: (a) chemical–mechanical polishing, (b) diamond paste polishing down to 0.25 μm, and (c) diamond paste polishing down to 1.0 μm [53].

Porous n-type 6H-SiC can be produced electrochemically using aqueous KOH in lieu of aqueous HF [58]. The etching process proceeds by oxide formation followed by dissolution of the silicon oxide. The flattest etched surface is attained at a current density of 1 mA/cm^2 in 1 wt% KOH at 50–55 °C under UV light illumination. Using this method, a patterned structure with evaporated Ni metal as the mask can be fabricated.

2.2. Luminescence from porous SiC

Compared to Si, silicon carbide has a wider band gap, 2.23 eV for 3C-SiC, 2.86 eV for 6H-SiC, and 3.0 eV for 4H-SiC [12], and so PL from SiC can be more easily shifted to a shorter wavelength as the particle size decreases to the nanometer regime. Therefore, SiC

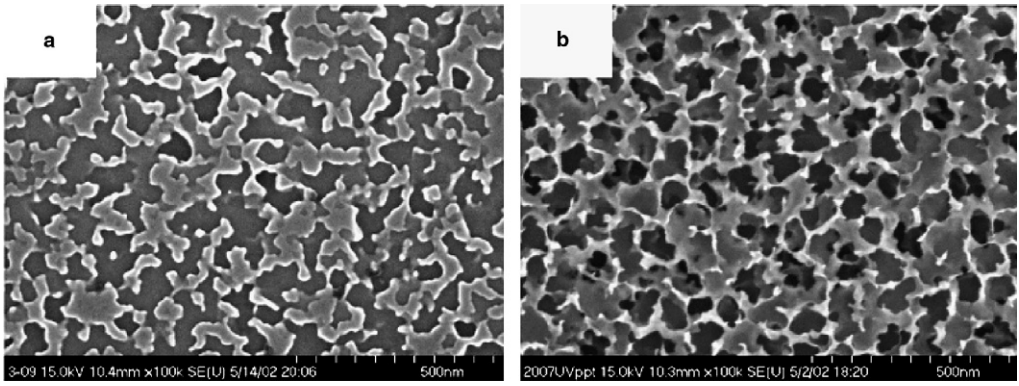

Fig. 5. SEM micrograph (plan view) of porous SiC prepared from n-type 6H wafer by electroless etching in concentrated HF etchant for (a) 20 min and (b) 60 min [57].

constitutes a better UV or blue emitter in applications such as light emitting diodes (LED) or displays. At the same time, SiC is one of the best biocompatible materials and has potential applications in biolabeling and biosensing [13,14].

It has long been known that bulk SiC can exhibit blue luminescence at room temperature. However, the emission intensity is rather low due to the indirect band gap. Since the mid-1990s, much work has been done to obtain more robust SiC quantum dots with controllable luminescent properties. Matsumoto et al. fabricated porous n-type 6H-SiC by means of electrochemical anodization in a HF–ethanol solution [15]. Fig. 6 shows the SEM image of the porous SiC layer showing many pores. The thickness of this layer after anodization for 60 min is about 3 μm.

In the luminescence spectrum, the peak is at around 460 nm, and the intensity is about 100 times higher than that of single crystal 6H-SiC (Fig. 7). Bulk 6H-SiC exhibits emission at a wavelength slightly longer than 600 nm, and this phenomenon is generally attributed

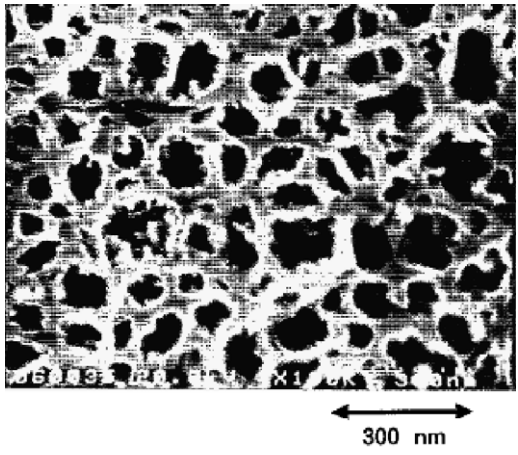

Fig. 6. SEM image of the porous SiC layer. The anodization current density is 40 mA/cm^2 [15].

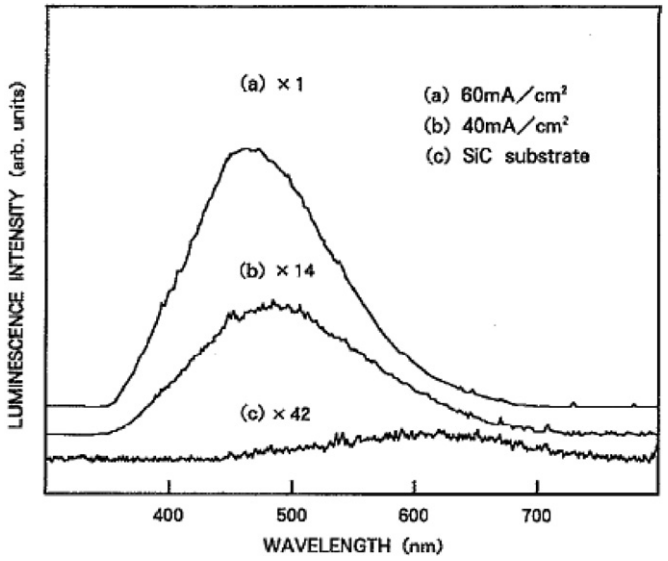

Fig. 7. Luminescence spectra acquired from porous SiC for an anodization current density of (a) 60 mA/cm^2 and (b) 40 mA/cm^2; (c) crystalline 6H-SiC [15].

to donor–acceptor recombination [59,60]. The observed luminescence is largely blue-shifted to 460–500 nm and the origin is believed to be different from that of bulk SiC. Moreover, the emission peaks (2.6–2.7 eV) lie below the band gap of bulk 6H-SiC, and so the effect cannot be induced by quantum confinement and may arise from some surface states generated during anodization.

Luminescent porous p-type 6H-SiC has been synthesized employing similar methods [16]. TEM micrographs indicate that the interpore spacings are between 1 and 10 nm and the average crystallite size is about 6 nm. The size is small enough that quantum confinement may emerge according to the theoretical calculation described in Ref. [61] (Fig. 8). Cathodoluminescence (CL) instead of PL has been conducted and the results are displayed in Fig. 9. An emission peak at 480 nm appears from both the SiC substrate and porous SiC. However, the intensity of the peak from the porous layer at 77 K is nearly three orders of magnitude lower than that from the substrate. The intensity of the peak from the SiC substrate decreases considerably at room temperature, while that of the porous SiC remains at about the same order of magnitude, resulting in an intensity ratio of 10:1 between them. This emission peak may originate from defect centers in 6H-SiC. With regard to the porous film, two new peaks emerge, one at 3.0 eV, and the other at 3.7 eV, and both of them are above the band gap of bulk 6H-SiC. Lowering of the anodization current density leads to the reduction or disappearance of these two UV bands. It is believed that they are possibly associated with recombination of carriers confined in the nanocrystals. However, the wavelength width at half maximum of both peaks is too small and they are too sharp, in contrary to the broad size distribution of the 6H-SiC nanocrystals as disclosed by TEM. Selected area diffraction (SAD) shows a pattern characteristic of single crystal in the porous SiC layer. This indicates that the unanodized portions of the porous layer are interconnected and maintain the original orientations, and it is in agreement with other reported results [47].

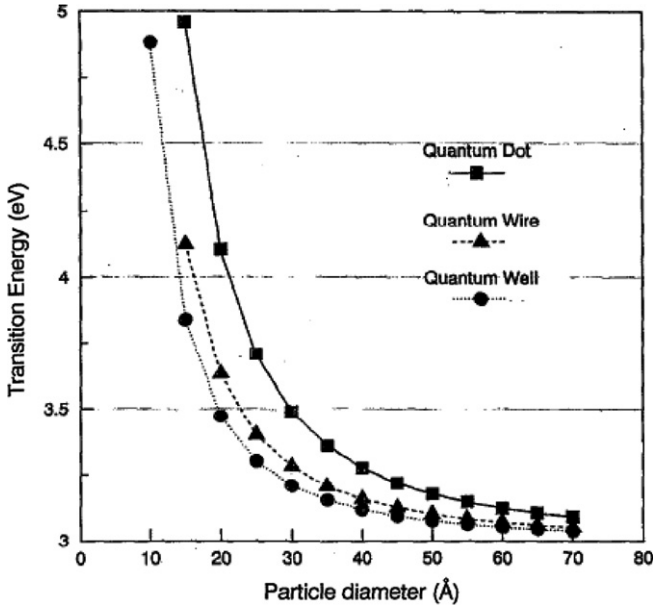

Fig. 8. Transition energy versus particle size for porous 6H-SiC [16].

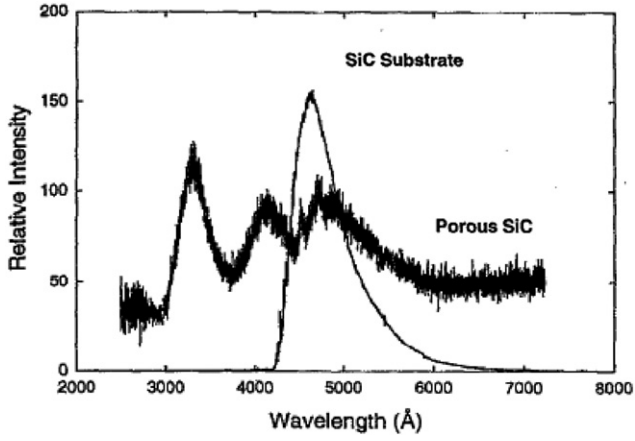

Fig. 9. Comparison of the CL between a UV luminescent porous p-type SiC film and substrate at 77 K. The porous film exhibits relatively weak luminescence, and the UV peaks which are present in the porous layer are absent in the substrate [16].

Another study of the luminescence from p-type 6H-SiC [17] shows that the PL of both the bulk and porous 6H-SiC are located at 2.65 eV (Fig. 10). They also have a similar line shape and this is consistent with the above-mentioned result [16]. However, the luminescent intensity from the porous sample is enhanced by about 100 times at 300 K rather than suppressed [16] compared to the bulk crystal, which agrees well with the general results observed in porous Si samples [6]. It is suggested that this luminescence originates from

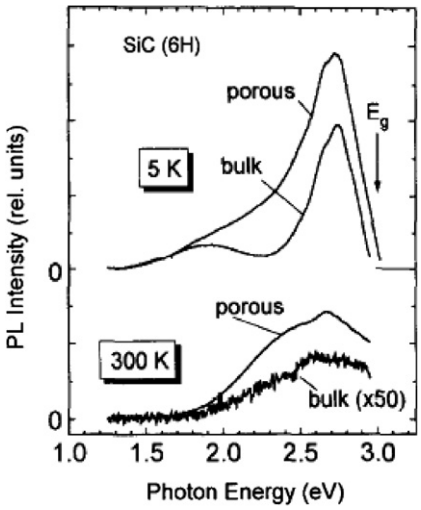

Fig. 10. PL spectra from bulk and porous 6H-SiC at 300 K and 5 K, with excitation energy of 3.5 eV [17].

the Al-related donor–acceptor. As expected, the PL intensity from bulk SiC increases largely and the peak becomes more defined when the temperature is reduced to 5 K. In comparison, there is further intensity increase of only about two times in porous SiC upon cooling from 300 to 5 K. As shown in Fig. 11, the EL spectra obtained from both samples have similar shapes and peak positions and the maximum enhancement is about 10 times. It should be noted that the PL band maximum of both samples appears at 2.25 eV rather than 2.65 eV. It is believed that the electrolyte excitation preferentially excites donor–acceptor pairs with a lower energy. The increased surface area between the porous layer and electrolyte may have led to the higher EL intensity compared to that of the bulk materials.

Very little is known about the surface compositions and structures of porous SiC. Free-standing layers with thicknesses between 5 and 40 μm have been fabricated [17], making it possible to obtain reliable infrared (IR) spectra. Fig. 12 shows the transmission spectrum

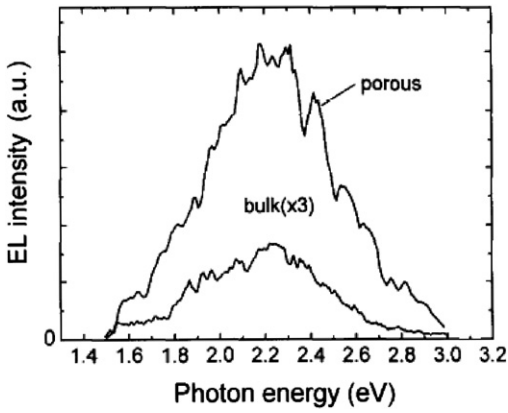

Fig. 11. EL spectra of bulk and porous 6H-SiC under forward bias in an electrolyte (0.15 M $Na_2S_2O_8$ + 1.0 M H_2SO_4) [17].

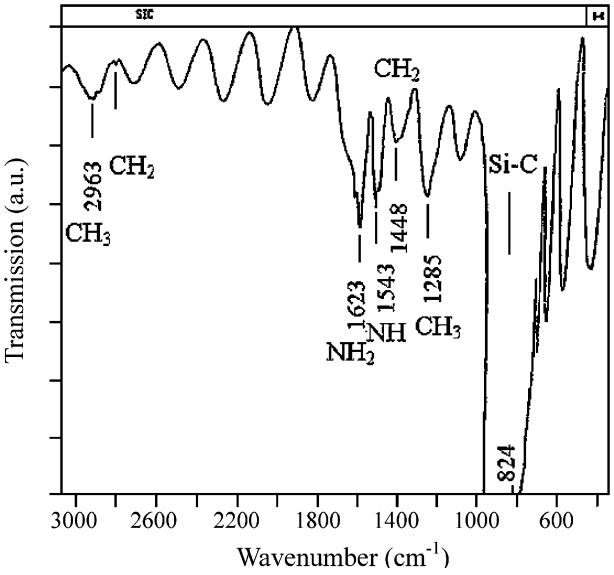

Fig. 12. IR transmission spectra of a typical free-standing porous 6H-SiC layer showing various vibration modes [17].

of such a porous 6H-SiC layer. The CH_2 and CH_3 stretching modes appear in the range of 2800–3000 cm^{-1}. The 1600 cm^{-1} peak is probably related to N–H vibrations that are quite strong in porous materials, indicating a high concentration of N and preferential attachment of H to these atoms. The 1448 and 1285 cm^{-1} peaks correspond to the CH_2 and CH_3 bending modes, respectively. The Si–C vibration modes appear at 800–1000 cm^{-1}. It should be noted that the Si–H peaks at 2100 and 2200 cm^{-1} are absent from the spectra, suggesting that H attaches predominantly to C. It may be induced by the existence of a carbon-rich phase on the surface of the electrochemically etched SiC by HF [20]. C–H bonds are known to resist oxidation thereby yielding stable surfaces.

In order to unravel the luminescent mechanism of the SiC crystallites, different polytypes of SiC and different fabrication conditions have been investigated [18]. N-type 6H-, 4H-, and 3C-SiC crystals are etched in NH_4F or HF at a current density of 2–5 mA/cm^2 either under UV irradiation or in the dark. The p-type samples are anodized at a current density of 50–60 mA/cm^2 in the dark. The obtained porous layer is about 5–10 μm. The average fiber size is 0.5–1 μm in samples prepared in the dark whereas it is less than 50 nm in samples fabricated using UV irradiation. The PL spectra from samples prepared with or without UV photoexcitation have similar shapes and emission wavelengths (Fig. 13), in contrast to the considerable differences in the electrical and physical properties [51].

No significant differences can be observed in the PL spectra acquired from samples fabricated under different conditions including electrolyte concentrations, etching time, applied bias, and photoexcitation. Therefore, the above results indicate that luminescence may be related to deep centers in the bulk SiC or surface states as a result of the large surface to volume ratio of the SiC crystallites. In order to identify the more dominant factor, comparative experiments have been conducted, as shown in Fig. 14, the PL spectra of different polytypes of SiC are quite similar.

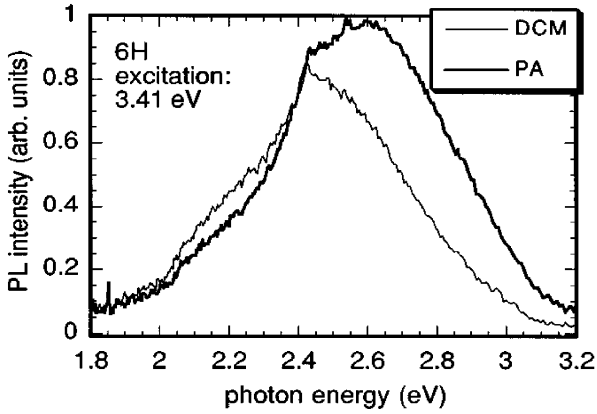

Fig. 13. Typical PL spectra acquired from porous SiC produced by anodization of n-type 6H-SiC with (PA) and without (DCM) UV photoexcitation [18].

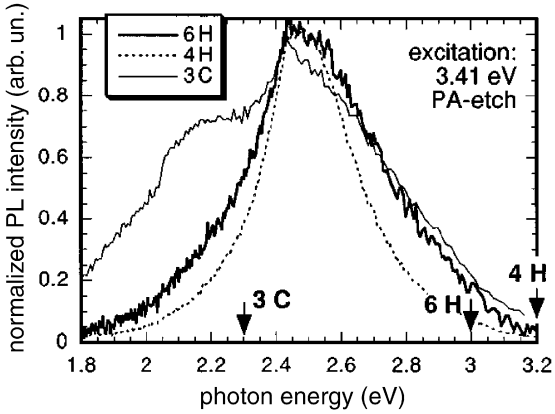

Fig. 14. Dependence of normalized PL spectra on the polytype of the initial crystal. The excitation wavelength is above the band gap for all the polytypes [18].

It is well known that the large band gap differences in 3C-, 4H-, and 6H-SiC lead to the 0.9 eV energy difference for the famous deep defect center, D_1, in these polytypes [62]. Therefore, it can be inferred that luminescence does not originate from D_1 or some typical bulk defects in crystalline SiC [59,60,63], as it does not depend on the polytype. It has been observed that annealing in oxygen at 700 °C for 1 h results in complete quenching of the PL (Fig. 15). The PL can be partially recovered by dipping the oxidized sample in 40% HF, probably because the HF-treated porous Si surface contains a carbon-rich phase giving rise to a high density of surface states [20]. The disappearance of PL upon oxidation and recovery via subsequent HF treatment suggest that luminescence from porous SiC should be related to the surface states.

The morphologies of anodized porous n-type and p-type 6H-SiC samples fabricated under different conditions and the PL properties have been studied [64]. Fig. 16 shows the SEM micrographs of the porous layer. The results obtained from the n-type porous

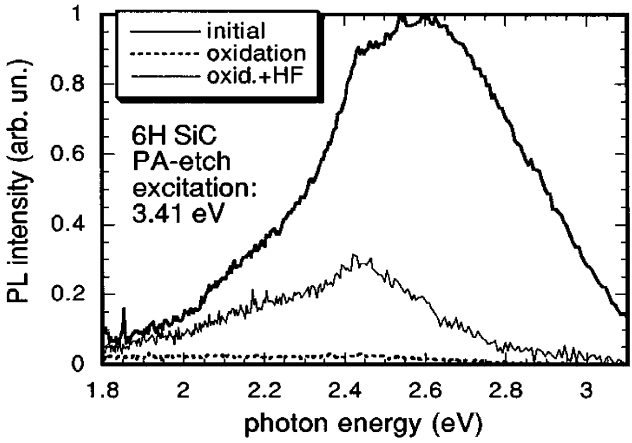

Fig. 15. Transformation of the PL spectra following thermal oxidation and subsequent treatment in HF [18].

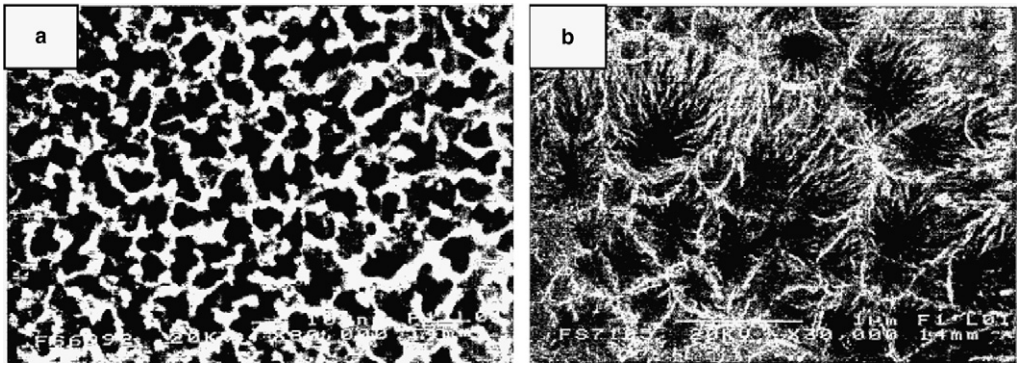

Fig. 16. SEM images of porous (a) n-type and (b) p-type SiC layers [64].

sample indicate that when the samples are etched under higher light intensity or higher HF concentration, the size of the walls is nearly unchanged, indicating that the ultimate size of the interconnected dots or wires is independent of the fabrication conditions. However, the pore diameters and porosity increase showing a strong dependence on these conditions. The results obtained from the p-type materials are quite different. After drying in air, the porous SiC layer delaminates from the substrate, but it can be prevented by supercritical drying in CO_2, similar to that of porous Si [65]. The SEM image in Fig. 16(b) shows that the dendritic morphology is quite different from that of the porous n-type sample.

Fig. 17 depicts the PL spectra acquired from both types of porous samples. The n-type substrate exhibits a peak at 2.2 eV which may be ascribed to defect centers. The porous sample displays an even broader band at about 2.6 eV with no clear dependence on the illumination density or the HF concentration. Meanwhile, the emission intensity of the original band at 2.2 eV is dramatically reduced. The p-type substrate shows a luminescence peak at 1.8 eV whereas the corresponding porous sample exhibits an emission peak at 2.5 eV that is close to that of the n-type porous sample. Since the typical interpore spacing

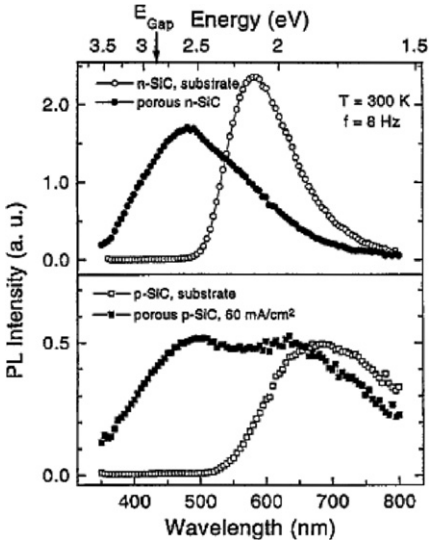

Fig. 17. PL spectra obtained from porous n-type (upper part) and p-type (lower part) 6H-SiC in comparison to the luminescence from the corresponding substrate [64].

in porous 6H-SiC (n-type) is 100 nm, the quantum confinement effect can be ruled out here. Thus the PL at 2.5–2.6 eV possibly arises from some surface states.

Other PL results have been obtained from porous SiC. For example, both the 6H-SiC substrate and corresponding porous sample have been observed to exhibit luminescence at about 600 nm, and the intensity is enhanced by about 100 times after etching [66]. In another piece of work, the CL spectra obtained from bulk 6H-SiC show emission at about 600 nm that is shifted to 355–400 nm for the porous samples [67]. Readers are referred to several other reports for more details on luminescence from porous SiC [68–74].

2.3. Common features

Luminescence from porous SiC prepared by electrochemical etching is discussed in this section. Almost all investigators have selected 6H-type SiC as the substrate. However, a more comprehensive study of the 3C, 4H, and 6H polytypes shows that there is no significant difference in the luminescent properties among these different porous samples [18]. The luminescent spectra acquired from porous SiC span a wide spectral range from near UV to about 600 nm. In some cases, the porous sample exhibits emission similar to that of the corresponding bulk materials [17,66], but in most cases, the porous samples exhibit new emission peaks shifted to the lower energy side relative to the PL peak of the substrate. The former emission may originate from intrinsic defect centers, whereas the latter is most likely associated with surface states created during the etching process. No explicit evidence of quantum confinement has been observed due to two reasons. First of all, the SiC crystallites fabricated in these experiments are too large, generally tens or hundreds of nanometers [15,17,18], for the appearance of quantum confinement. Crystallites with sizes of several nanometers had, however, been once reported [16] but no obvious signs of quantum confinement have been obtained. Research has revealed that the porous SiC etched in

aqueous HF has a carbon-rich layer on which complicated surface states can appear [17]. They may be responsible for the observed luminescence similar to that of porous Si [75–77].

3. SiC nanocrystals embedded in matrix

3.1. C ion implantation into crystalline Si

A porous 3C-SiC layer can be produced via anodization of annealed carbon implanted Si [19]. In this experiment, carbon ions are first implanted into a boron-doped Si wafer with a dose of 10^{17} cm^{-2} and then annealed in N_2 at 950 °C for 1 h. The sample is subsequently anodized using a current density of 40 mA/cm^2 in an HF–ethanol solution for 10 min while illuminated from above by a 150 W halogen lamp to expedite the etching process. The PL spectra obtained from the implanted and unimplanted samples are displayed in Fig. 18. The unimplanted sample shows an emission peak at 560 nm (2.2 eV) which is typical of porous Si and may be ascribed to Si nanocrystals [6]. With regard to the C ion implanted Si sample, a new emission band appears at 445 nm (2.79 eV) in addition to the peak at 560 nm. Its intensity is much higher than the Si-related emission band and it is thus an implantation related effect.

The FTIR spectrum shows an absorption peak at about 800 cm^{-1} corresponding to the TO phonons in 3C-SiC [78]. To further understand the PL peak at 445 nm, cross-sectional TEM is conducted. As shown in Fig. 19 [79], the implanted and annealed sample has three layers: (A) a damaged single crystalline Si layer that is 90 nm thick, (B) a 60-nm thick polycrystalline layer, and (C) a 50-mm thick solid-phase epitaxial layer. The HRTEM images reveal that 3C-SiC nanoparticles with sizes of 2–8 nm are formed epitaxially in layers A and C, but are randomly dispersed in layer B [79,80]. The in-depth distribution of the

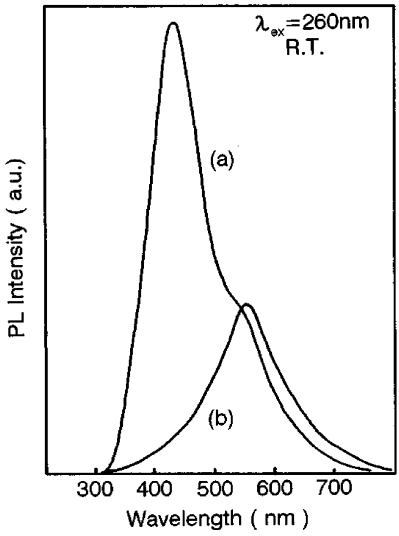

Fig. 18. PL spectra acquired from: (a) C ion implanted sample after annealing, and (b) reference sample without ion implantation. Both samples are anodized at 40 mA/cm^2 for 10 min [19].

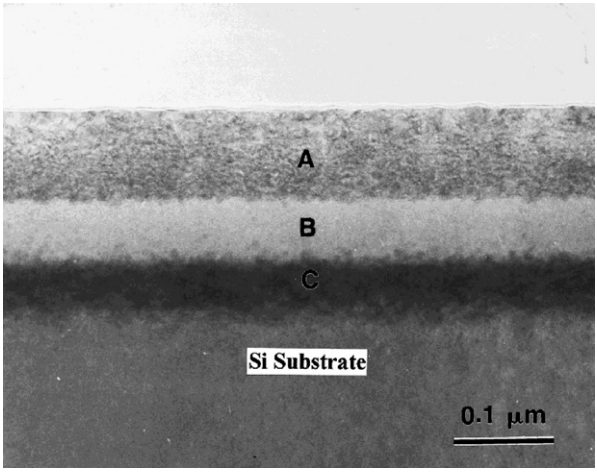

Fig. 19. Cross-sectional TEM micrograph acquired from the C ion implanted single crystal silicon sample after annealing in N_2 at 1100 °C for 90 min. The surface of the sample contains three layers, A, B, and C, with different contrasts [79].

3C-SiC particles resembles a Gaussian distribution indicative of ion implantation. The PL peak energy (2.79 eV) of the porous 3C-SiC sample is higher than that of the band gap of bulk 3C-SiC that is 2.2 eV [12]. This phenomenon may stem from quantum confinement in the porous 3C-SiC, but no further evidence has yet been obtained. SiC nanoparticles can be encapsulated in ZSM-5 (a kind of Si–Al zeolite with a two-dimensional open framework structure with 50–60 nm pores) by carbon ion implantation into the Si/ZSM-5 host–guest composite materials followed by thermal annealing in a vacuum chamber [81]. The emission peaks are centered at 548 and 460 nm, respectively, and the 460 nm peak is conjectured to arise from SiC.

3.2. SiC embedded in SiO_2

There have been several reports on embedding Si nanocrystals into SiO_2 films to generate visible PL [82,83]. Due to the much larger band gap of bulk SiO_2 (9.3 eV) [84] compared to that of Si (1.12 eV) [12], carriers can be confined in the Si crystallites. Luminescent SiC nanocrystals embedded in SiO_2 matrix can be realized similarly.

Thermal SiO_2 films have been co-implanted with Si and C to obtain intense, short wavelength PL [22]. Si ions are first implanted followed by 1100 °C annealing for 60 min. Then C ions are implanted to the same depth and the sample is further annealed. The sample annealed at 800 °C for 60 min shows a dominant peak at 470 nm and a weaker peak at 350 nm (Fig. 20). As the annealing temperature is increased, the PL intensity goes up. By comparing the PL spectra and the PL dynamics to those of Si or C ion implanted SiO_2 films, it can be deduced that the interaction between Si and C in the SiO_2 films plays an important role in the luminescence from the co-implanted films.

Si and C co-implanted SiO_2 films can exhibit even more complicated emission bands. In fact, as shown in Fig. 21, white luminescence has recently been reported [85]. These structures are synthesized by sequential Si^+ and C^+ implantation followed by high temperature

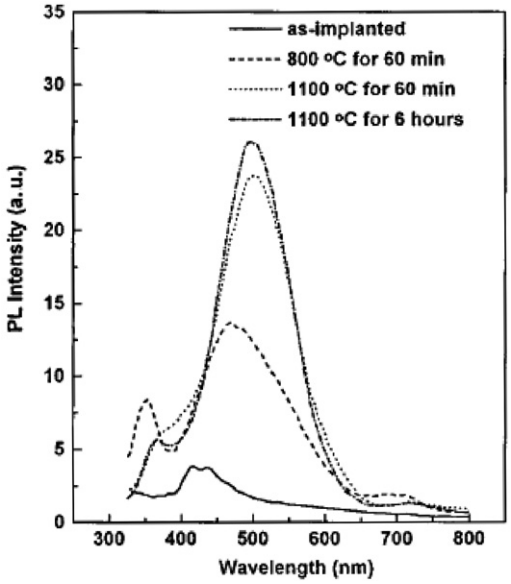

Fig. 20. Room temperature PL from C^+ and Si^+ co-implanted and annealed SiO_2 films at an excitation wavelength of 300 nm [22].

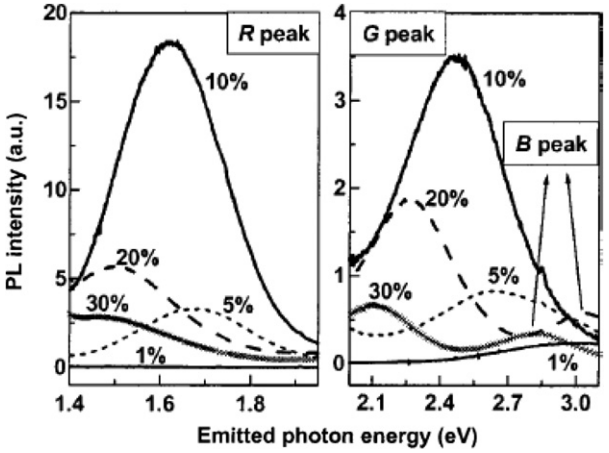

Fig. 21. PL spectra obtained from samples implanted with different fluences of Si and C. The samples are annealed at 1100 °C for 2 h [85].

annealing. The white emission is the result of the co-existence of three bands in the PL spectra covering the whole visible spectral range. Microstructural characterization reveals the presence of a complex multilayer structure. The Si nanocrystals are observed only outside the main C-implanted peak region. The density and size of the nanocrystals are smaller closer to the surface. These nanocrystals appear to be responsible for the emergence of the band in the red region of the PL spectrum. The relationship between the higher energy

bands with the implantation fluence and annealing time suggests that they are related to the formation of carbon-rich precipitates in the implanted region. In comparison, two emission peaks at 2.1 and 2.7 eV are observed from thin, thermally grown SiO_2 layers implanted with silicon and carbon ions [86]. $Si_yC_{1-y}O_x$ complexes with $x < 2$ are assumed to cause the observed blue PL.

3C-SiC nanocrystals have been prepared by carbon implantation into Si followed by annealing in Ar and dry oxidation [87]. Two PL bands at 460 and 535 nm are detected. The carbon-implanted thermal SiO_2 films also exhibit blue luminescence centered at about 490 nm [88]. The PL peak location and intensity depend strongly on the annealing temperature. HRTEM measurements reveal the formation of amorphous carbon clusters which may be the origin of the observed PL.

SiC–SiO_2 composite films can be formed by co-sputtering of SiC and SiO_2 [89]. The films show a PL band at 460 nm (2.7 eV). The intensity increases and then decreases with increasing annealing temperature. The as-deposited SiC–SiO_2 composite films are amorphous but SiC nanocrystals with diameters of about 5 nm can be observed in the 740 °C annealed samples. The FTIR spectra of the as-deposited film show a SiC absorption peak at 803 cm^{-1} and Si–O stretching band at 1030 cm^{-1}. The origin of the luminescence is suggested to be related to defects in the silicon oxide at the SiC/SiO_2 interface.

Methane plasma immersion ion implantation (PII) into silicon has been used to produce SiC [90]. The hydrogenated amorphous silicon carbide is transformed into 3C-SiC at high annealing temperature. The FTIR spectra show that the amount of Si–C bonds increases with annealing temperature while that of the C–C bonds decreases. At a high temperature, a large amount of 3C-SiC forms and graphitization occurs in the remaining carbon clusters. The CH_4 implanted and annealed samples show a PL peak at about 450 nm which may be related to the 3C-SiC grains.

3.3. Other methods

This section reviews several other methods used to produce SiC nanocrystals that emit visible light. Several groups have reported the formation of SiC films by deposition of C_{60} films on Si substrate followed by thermal annealing [91–94]. The deposited C_{60} is progressively destroyed by annealing, and then carbon reacts with silicon to form SiC [94]. The reaction starts at the interface and continues by diffusion of silicon through the formed SiC. The stoichiometric films are uniform with a grain size of 20–40 nm. In a similar way, blue light emitting 3C-SiC has been fabricated by annealing C_{60}-coupled porous silicon [23]. The C_{60} molecules are chemically incorporated into the porous Si structure by means of a coupling agent [$(CH_3O)_3Si(CH_2)_3NH_2$], as shown in Fig. 22. To prevent the C_{60} molecules from escaping during high temperature annealing, a 1 μm thick Si film is first deposited on the C_{60}-coupled porous Si by magnetron sputtering. The sample is then annealed in nitrogen at 1100 °C for 100 min. During annealing, the coupling agent and C_{60} molecules are decomposed and react with Si to form SiC crystallites. FTIR and XRD spectra obtained from the samples indicate the formation of 3C-SiC. Fig. 23 shows the PL spectrum which can be deconvoluted into two peaks at 450 and 380 nm. The 380 nm peak is frequently observed from Si oxide films prepared by magnetron sputtering [95,96] and is considered to be associated with SiO_2. The 450 nm peak is believed to derive from the a-$Si_{1-x}C_x$:H components.

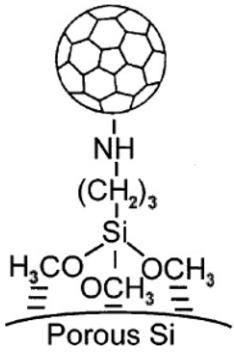

Fig. 22. Schematic diagram of the porous Si/C_{60} coupling system [23].

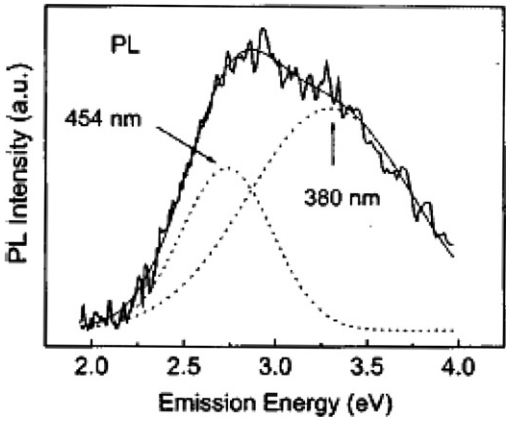

Fig. 23. Typical PL spectrum acquired from the Si-coated and annealed sample. The spectrum can be deconvoluted into two Gaussian distributions centered at 380 and 454 nm [23].

By means of high temperature pyrolysis of a polyimide Langmuir–Blodgett film on porous silicon in vacuum, 3C-SiC layers can be formed [97]. The blue–green luminescence is believed to come from the silicon carbide layers. The SiC/porous Si films can also be formed by plasma sputter deposition on porous Si using a SiC target [98]. The thin SiC film (~50 nm) mitigates the intensity of the 700 nm PL peak by up to three times compared to the uncoated porous Si. This band originates from porous Si. In addition, an emission peak at 450 nm appears and is ascribed to the SiC film or SiC nanoclusters.

Silicon or silicon dioxide films are used as the substrates in the aforementioned processes and SiC nanoclusters are formed at high temperature. Silicon carbide can also be formed by Si ion implantation into diamond [99,100]. In this process, natural IIa diamond is implanted with 1×10^{15} cm^{-2} nitrogen at 90 keV and then with 3×10^{17} cm^{-2} silicon at 150 keV at a temperature of 900 °C. A buried epitaxial layer with crystalline 3C-SiC subsequently forms, and by elevating the temperature during implantation, amorphization and graphitization can be prevented. The implanted region has a lower electrical resistivity [99]. The cross-sectional XTEM image of the sample implanted at 1200 °C is displayed in

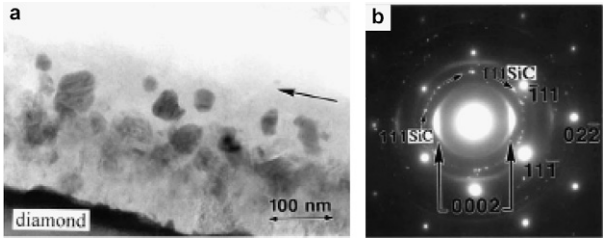

Fig. 24. (a) Bright field XTEM image and (b) selected area electron-diffraction (SAED) pattern obtained from natural diamond implanted with 1×10^{18} cm^{-2} Si at 1200 °C. The diamond is turned to graphite in the 220 nm thick top layer and the surface is marked by an arrow. SiC is formed in the region with the polycrystalline grains [100].

Fig. 24(a) [100]. A ~220-nm thick implanted zone together with an amorphous matrix comprising crystalline grains of SiC up to 50 nm in diameter can be observed. The selected area electron diffraction (SAED) pattern shows the formation of 3C-SiC within a stripe of textured graphite as shown in Fig. 24(b). The ring with many small diffraction dots indicates that the 3C-SiC domains are more or less randomly oriented. No luminescence has, however, been reported from these silicon implanted diamond samples.

4. Chemical vapor synthesis of SiC nanocrystals

Chemical vapor deposition (CVD) is another common method to prepare SiC nanocrystals. By thermal decomposition of the $(CH_3)_4Si$ precursor in a hot wall tube reactor at reduced pressure, SiC nanoparticles with sizes between 3 and 10 nm have been produced [101]. The materials synthesized at 1000 °C are completely amorphous, although individual nanometer-sized clusters can be distinguished. However, as illustrated in Fig. 25, the

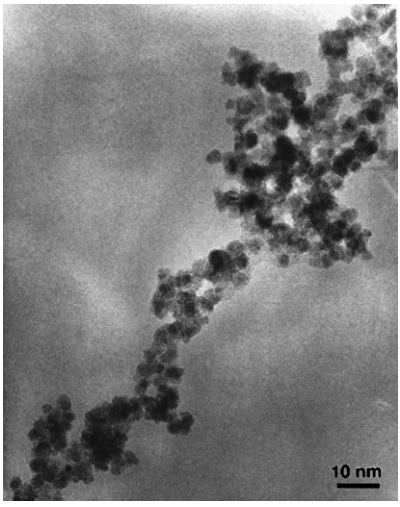

Fig. 25. Low magnification image of CVD SiC showing individual clusters with sizes ranging from 3 to 10 nm [101].

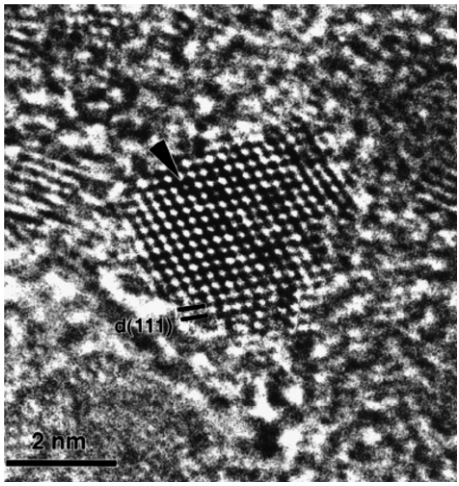

Fig. 26. SiC nanoparticle exhibiting very few stacking faults. The reaction pressure is 8 mbar. The site with the typical HREM contrast due to the presence of a defect is indicated by an arrow [101].

materials appear as crystalline at 1100 °C. The clusters are embedded in an amorphous matrix which consists mainly of carbon. The number of crystalline particles increases with temperature. High resolution electron microscopy investigation of individual nanoparticles confirms the crystalline characteristics (Fig. 26). Stacking faults can also be identified but they gradually disappear at lower reaction pressures. It should be noted that the reaction temperature and pressure only influence the crystalline quality but not their sizes.

The Raman spectra of quasi-stoichiometric SiC nanoparticles have been studied [102]. SiC nanoparticles are synthesized by CO_2 laser pyrolysis of a gaseous reactant mixture of silane (SiH_4) and acetylene (C_2H_2) [103]. TEM confirms the homogeneous composition of the SiC nanopowders with a narrow particle size distribution with an average size of about 10 nm (Fig. 27(a)). The high-resolution TEM images reveal that each particle consists of several crystallites with sizes of about 2.5 nm embedded in an amorphous SiC matrix (Fig. 27(b)). Si magic angle spinning (MAS)-NMR (nuclear magnetic resonance) measurements show the coexistence of amorphous, hexagonal, and cubic SiC structures. To modify the particle surface states via the elimination of excessive residual carbon and surface dangling bonds, the samples are annealed for 1 h under a continuous flow of oxygen at 440, 550, and 970 °C. The IR spectra show the appearance of Si–Si and Si–O bonds but the Si–C bonds can still be observed up to a temperature of 970 °C. The Raman spectrum consists of a broad peak from 514 nm to 800 nm with the peak at about 560 nm and this arises from PL (Fig. 28). The highest PL intensity is obtained on the sample oxidized at the highest temperature. The results show that the higher the fraction of the amorphous structure in the SiC nanoparticles, the higher is the PL signal. Hence, it is believed that the visible PL originates from the amorphous portion of the SiC nanoparticles as well as the heterogeneous oxygen-rich surface. Using the SiC powders, SiC/PMMA (polymethyl-methacrylate) composite films have been produced and the materials show the electro-optic phenomena of electrically poled films (0.5 μm) [104].

In 1975, Yajima reported a preceramic polymer route to prepare β-SiC fibers industrially [105,106]. Recently, silicon carbide nanostructures have been synthesized utilizing a

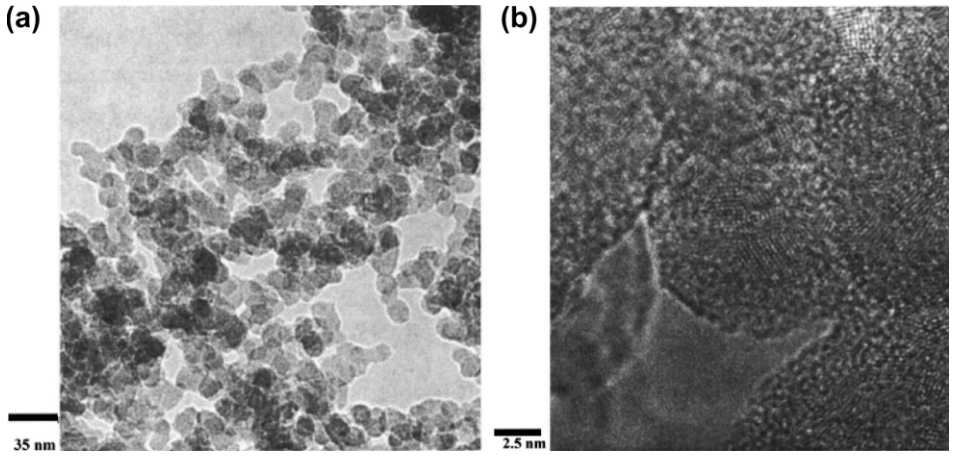

Fig. 27. TEM images of the SiC powder sample: (a) low-resolution image indicating the homogeneous particle with diameters of about 10 nm and (b) high-resolution image of a nanoparticle composition showing an amorphous background and nanocrystal diameter of about 2–3 nm [102].

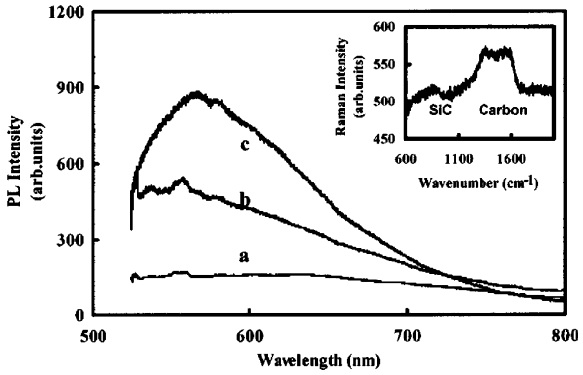

Fig. 28. Broad PL bands in the Raman spectra acquired from the SiC samples: (a) as-formed sample, (b) sample heated to 440 °C under oxygen, and (c) sample heated to 970 °C under oxygen. The intensities are normalized by weight factors of 1/3 (a), 1 (b), and 1/10 (c). The inset shows the Raman spectrum of the as-formed sample with vibrational bands from carbon and SiC [102].

simplified Yajima process [107]. NaH powders are decomposed to form small droplets of liquid Na at 623 K and under 1 atm of Ar. Afterwards, the reaction between liquid Na and $SiMe_2Cl_2$ or $SiMeCl_3$ vapors generates particle precursors Pre-I and Pre-II, respectively. The precursors are then decomposed at 1273 K under vacuum to produce fine powders as the final products. Black powder I and yellow powder II are produced from Pre-I and Pre-II, respectively. Two types of particles are identified in powder I and their SEM and TEM micrographs are depicted in Fig. 29. The dominant particles, Ia, manifest as hollow cubic cages with edge lengths of 60–400 nm (Fig. 29(A) and (C)). The minor particles, Ib, are cubes with a length of 1–2 μm (Fig. 29(B) and (D)). The electron diffraction (ED) patterns indicate that Ia and Ib are polycrystalline β-SiC. Electron microscopy

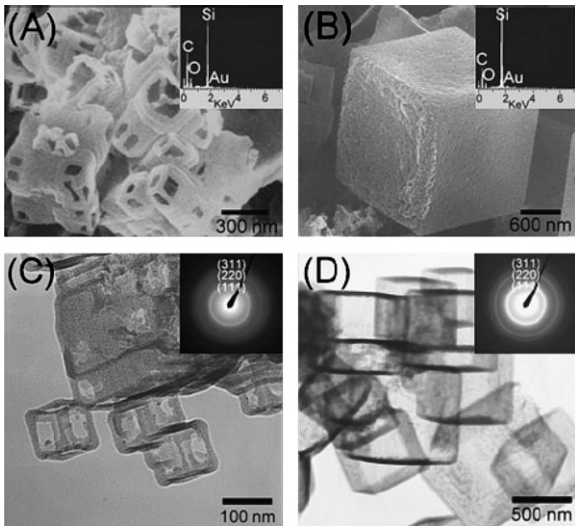

Fig. 29. Images of I, prepared from $SiMe_2Cl_2$ and Na. SEM images and energy dispersive spectroscopy (EDS) spectrum (insets) of (A) Ia; (B) Ib. Transmission electron microscopy (TEM) images and electron diffraction (ED) patterns (insets) of (C) Ia; (D) Ib [107].

images show that powder II consists of spherical nanoparticles with an average diameter of about 10 nm and electron diffraction also reveals the polycrystalline nature of powder II. Both the precursors in Pre-I and Pre-II are composed of mixtures of polycarbosilane and NaCl, and it is believed that the distinct shape variations in the final products of β-SiC arise from the differences in the precursors.

5. Colloidal 3C-SiC nanocrystals and evidence of quantum confinement

The composite structures containing SiC crystallites described so far have a solid structure, for example, interconnected SiC nanowires, nanocrystals in porous SiC, or SiC particles embedded in a solid matrix. Unfortunately, owing to the complicated surface states, quantum confinement effects have not been clearly demonstrated from these nanostructures. Therefore, a different preparation method is needed to fabricate SiC nanostructures in order to realize wavelength-tunable and controllable luminescence with the quantum confinement effect. Recently, intense luminescence showing unequivocal quantum confinement has been observed from 3C-SiC suspensions [33].

5.1. Fabrication

A procedure for generating colloidal suspensions of Si exhibiting luminescence attributable to quantum confinement has been reported [25]. N- or p-type Si wafers are electrochemically etched to form porous Si and then ultrasonically dispersed in methylene chloride, acetonitrile, methanol, toluene, or water to form a suspension consisting of luminescent Si particles. The TEM micrographs show that the Si particles have regular shapes and diameters ranging from several nanometers to micrometers. Although quantum-sized Si particles can also be synthesized from silane by means of slow combustion [108], microwave plasma

[109], or chemical vapor deposition [110], these methods tend to produce impure Si crystallites containing a large amount of SiO_2, whereas porous Si prepared in an HF electrolysis bath has a clean, H-terminated surface that contains no SiO_2 [111,112]. Hence, in comparison with gas-phase preparation of colloidal Si, this technique produces Si crystallites from high-purity substrates and avoids contamination by SiO_2 and other impurities. Upon excitation by the 442 nm line of a 10 mW He/Cd laser, the suspension exhibits emission with the maximum wavelength varying between 650 and 750 nm [25] depending on the different solvents and preparation procedures. The full width at half maximum (FWHM) is typically 200 nm. These emission spectra qualitatively match those of the solid samples before dissolution as well as those obtained from plasma-deposited Si nanoparticles [109].

A similar strategy has recently been adopted to synthesize colloidal 3C-SiC nanocrystals [33]. The 3C-SiC polycrystalline samples are electrochemically etched in HF–ethanol ($HF:C_2H_5OH = 2:1$) under illumination by a 150 W halogen lamp from above. The obtained porous 3C-SiC is then treated in an ultrasonic bath. During the process, the porous layers on the surface crumble into small crystallites which disperse in the solution. Fig. 30(a) shows a TEM image of the nanocrystallites from one such sample produced at an etching current density of 60 mA/cm^2. It can be seen that the crystallites are almost spherical with diameters ranging from 1 to 6 nm. The high resolution TEM image clearly shows the lattice fringes which can be assigned to the {1 1 1} plane of 3C-SiC [Fig. 30(b)].

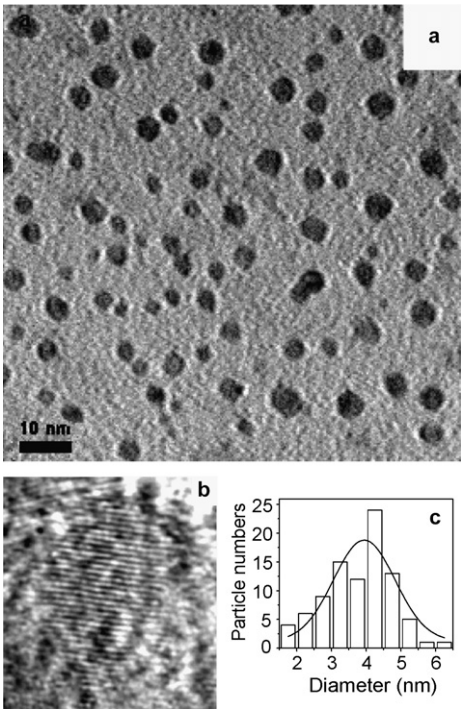

Fig. 30. (a) TEM image of the sample fabricated using an etching current density of 60 mA/cm^2. The nanocrystallites are nearly spherical. (b) HRTEM image of one particle. The lattice fringes corresponding to the {1 1 1} plane of 3C-SiC can clearly be identified. (c) The particle number histogram showing with an average size of 3.9 nm based on Gaussian fitting [33].

Fig. 30(c) displays the size distribution of the particles. A Gaussian fit puts the median diameter at about 3.9 nm. The samples fabricated using different etching current densities between 70 and 20 mA/cm^2 have similar size distributions. One sample that is prepared specially by multiple etching using different current densities (see Ref. [33] for details) contains particles having a narrower distribution with larger average size. It should be noted that the colloidal 3C-SiC particles fabricated have a more regular shape compared to Si crystallites produced by similar means [25]. This may be because polycrystalline rather than single-crystal 3C-SiC is used.

5.2. Photoluminescence and evidence for quantum confinement effect

The aqueous suspension of the 3C-SiC crystallites exhibits intense emissions as shown in Fig. 31(a). The spectral lines are smooth and have no substructures, with a typical wavelength width at half maximum of about 120 nm. As the excitation wavelength increases from 250 to ~500 nm, the emission wavelength is continuously shifted to red from ~450 to ~540 nm [Fig. 31(b)]. However, no emission can be observed if the excitation wavelength is longer than ~500 nm. This can be explained by the quantum confinement effect. The suspension contains 3C-SiC particles of different sizes with an approximate Gaussian distribution [Fig. 30(c)]. Smaller particles have larger band gaps as expected from the quantum confinement effect [8,9]. As the excitation wavelength increases, carriers in many small particles cannot be excited leading to the observed continuous redshift. When the excitation wavelength reaches ~500 nm, only the largest particles which have the smallest band gap can be excited. In fact, the emission wavelength, ~540 nm, is close to the band gap of bulk 3C-SiC which is 556 nm (2.23 eV) [12]. If the excitation wavelength increases further (>~500 nm), no particles can be excited, and naturally, no luminescence emerges. The upper flat line in Fig. 31(b) shows the PL peak wavelength of the specially fabricated sample which contains much larger 3C-SiC particles. They are too large to exhibit quantum confinement, and so the emission wavelength remains almost constant at ~550 nm under different excitations.

The emission intensities of the above samples fabricated using different current densities increase initially and then decrease with increasing excitation wavelengths. The maximum

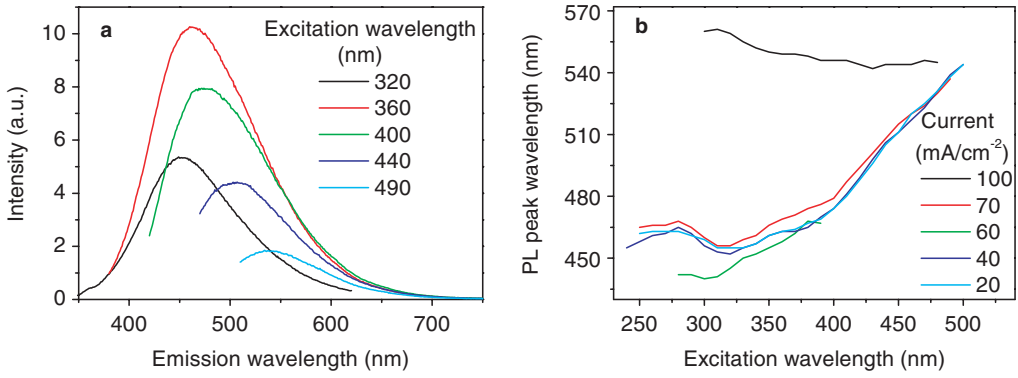

Fig. 31. (a) PL spectra taken under different excitation wavelengths from the sample fabricated using a current density of 40 mA/cm^2. (b) PL peak position versus the excitation wavelength for samples produced using different etching current densities [33].

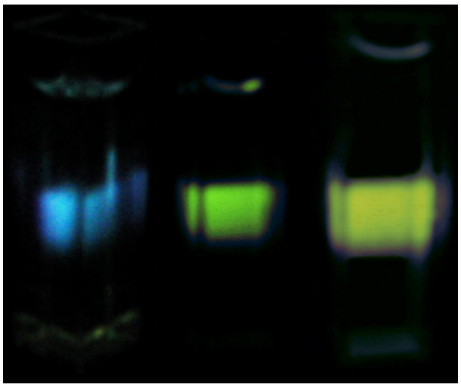

Fig. 32. Emission photos from the sample fabricated with a current density of 40 mA/cm^2 (left and center) and from the specially fabricated sample (right) under excitation wavelengths of 320, 400, and 450 nm [33].

value occurs at an excitation wavelength of around 370 nm. The results further demonstrate the size distribution of the crystallites shown in Fig. 30(c) and corroborate quantum confinement. The emission intensity from the specially fabricated sample is much lower compared with that from the above-mentioned samples and increases slowly due to the low emission efficiency of the bulk materials. In fact, emission from the 3C-SiC suspensions that is visible to the naked eyes is much stronger than that from the Si suspensions fabricated under similar conditions. Fig. 32 shows the emission photo taken under different excitations using a halogen lamp.

Although luminescent 3C-SiC suspensions have been prepared utilizing methods similar to that for the fabrication of colloidal Si [25], there are some differences. For instance, although the as-etched porous Si exhibits luminescence with the quantum confinement effect and the PL from colloidal Si is similar to that of the as-etched sample, the as-etched porous 3C-SiC shows no detectable luminescence but the colloidal 3C-SiC crystallites show luminescence with quantum confinement. There are two possible reasons. Firstly, the as-etched porous SiC contains interconnected particles which cannot exhibit quantum confinement effects. After the ultrasonic treatment, the networks are destroyed forming individual crystallites with sizes of several nanometers that are small enough to exhibit quantum confinement. Secondly, water provides good surface passivation for the particles. Both factors are believed to play important roles in the observed luminescence.

5.3. 3C-SiC/polystyrene composite films

Solid luminescent films may be more useful in practical applications, and 3C-SiC/polystyrene composite films have been successfully produced using colloidal 3C-SiC particles [36]. A 3C-SiC suspension in toluene exhibits wavelength-tunable emission similar to the aqueous suspension. Polystyrene is added to the suspension and the solution is put on a Si wafer to produce a transparent 3C-SiC/polystyrene film. Fig. 33 shows the emission spectrum acquired from the composite film at an excitation wavelength of 325 nm. Since pure toluene and polystyrene show no luminescence, the observed emission from the 3C-SiC/polystyrene film should originate from the 3C-SiC particles surrounded by polystyrene. The luminescence is visible to the naked eyes, although it is noticeably less intense than that

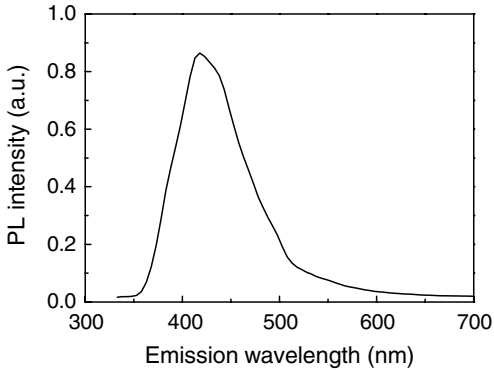

Fig. 33. Emission spectrum acquired from 3C-SiC nanocrystallites in a polystyrene film excited by the 325 nm line of a He–Cd laser [36].

from the original SiC suspension in toluene that does not contain polystyrene. It is possibly because the SiC nanocrystallites are only partially enclosed by polystyrene in the composite film. The emission shows a blueshift of about 15 nm compared to the original 3C-SiC suspension of toluene. A larger blueshift has been observed from the Si/polymer films and it can be attributed to oxidation of the particle surfaces during the casting process [25]. However, SiC cannot be easily oxidized at room temperature, implying that smaller particles that are more easily enclosed by polystyrene may account for the blueshift.

6. Theoretical investigation of the electronic structures of SiC quantum dots

As described in the previous section, much experimental research has taken place to investigate the luminescence and optical properties of SiC nanocrystallites, but on the other hand, relatively few theoretical studies have been carried out. In this section, we succinctly review the theoretical investigations conducted on SiC nanocrystals.

The dependence of the band gap of 6H-SiC on size has been derived [16] using a model for porous Si [61]. The model assumes that the porous materials are composed of quantum dots, wires, or wells, and that the carriers are confined by an infinite square-well potential. The eigenenergies of the electrons and holes obtained by solving Schrödinger's equation for one, two, and three dimensions are added to the band gap to obtain the transition energy, which is the effective band gap of the nanocrystallites. The transition energy of the 6H-SiC crystallites as a function of the particle sizes can then be derived (Fig. 8). The results show that particles smaller than 3 nm exhibit significant band-gap widening, and this effect is minimal in particles between 4 and 7 nm. However, due to gross simplification, the model should only be considered qualitative.

The exciton ground states in 3C-SiC quantum dots have been investigated using the effective mass theory [34] by taking into account the conduction- and valence-band mass anisotropy as well as the small spin–orbit splitting energy. The degenerate hole and exciton states are partly split by the mass anisotropy. Due to quantum confinement, the anisotropy splitting energies in the quantum dots are quite different from their bulk values. The anisotropy and exchange splitting lead to the splitting of the 48-fold exciton ground state into two 18-fold triplets and two 6-fold singlets. Fig. 34 shows the exciton band gap versus dot radius for 3C-SiC quantum dots. The band gap increases with decreasing

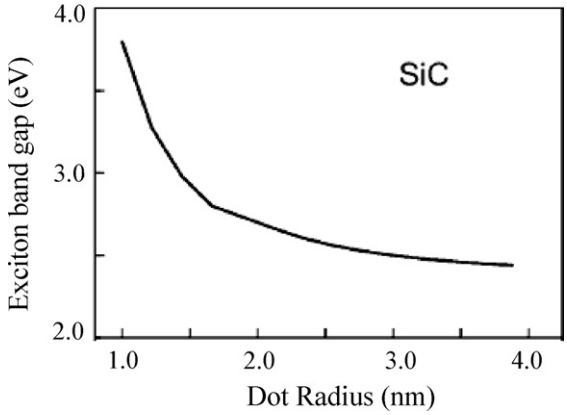

Fig. 34. Exciton band gap versus dot radius for 3C-SiC quantum dots [34].

particle size, and it is especially obvious below 4 nm. It is because of the quantum confinement effect and a smaller dielectric constant of the quantum dots. Stable exciton states exist even at room temperature in a 3C-SiC quantum dot because of the strongly bound electron–hole pair. In comparison, this only occurs at low temperature in the bulk materials.

An ab initio study of the stability and optical gaps of 3C-SiC quantum dots has recently been conducted [37] using the density functional theory in conjunction with gradient corrected approximation [113]. A cubic 3C-SiC core structure is assumed for each dot and six different surface geometries including three different terminations (C, Si, or Si-rich) as well as two different surface structures of ideally terminated or reconstructed (1 0 0) facets (with dimer formation) are considered. For each cluster, after the initial core cubic geometry is set, all the atomic coordinates are optimized using damped molecular dynamics or conjugate gradient algorithms. Fig. 35 shows the electronic gaps obtained from several SiC

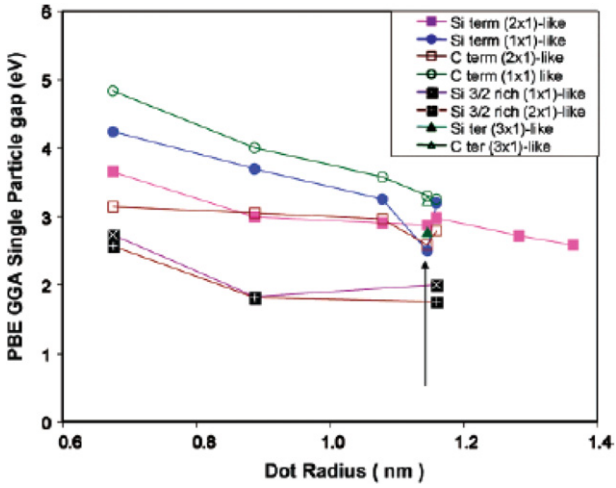

Fig. 35. Single-particle electronic gap of SiC quantum dots as a function of size for different surface structures. The gap is computed employing generalized gradient corrected approximation (GGA-PBE) [37].

clusters with different terminations as a function of the difference between the lowest unoccupied molecular orbital (LUMO) and the highest occupied molecular orbital (HOMO) eigenvalues. Other works on Si and C indicate [114,115] that the HOMO–LUMO energy difference underestimates the optical gap of the quantum dots when compared to more accurate methods such as quantum Monte Carlo (QMC). However, the HOMO–LUMO and QMC gaps show the same qualitative trend as a function of particle size and surface structure. Fig. 35 discloses that the band gap increases generally with reduced quantum dot size, but it also depends strongly on the surface structure. Generally, the C-terminated and H-rich quantum dots have the largest gap. Calculations indicate that the optical gap depends on the structural properties of the dots at the surface and within the bond lengths of the nanoparticle core. Analysis of the free energy of the SiC dots shows that synthesis of thermodynamically stable, hydrogenerated SiC dots will lead to only two specific types of particles: dots with (1×1) C-terminated surfaces or dots with (2×1)-reconstructured Si-terminated surfaces.

7. Luminescence from SiC thin films

SiC films such as 3C-SiC produced by chemical vapor deposition (CVD) are potential materials in optoelectronic applications such as flat panel displays, and their PL properties have recently been evaluated. A detailed PL study has been conducted at 2 K on a series of CVD 3C-SiC thin films fabricated on (1 0 0) Si substrates with thickness between 60 nm and 25 μm [42]. The "defect-related" W band near 2.15 eV appears from the very thin films. The G band at 1.90–1.92 eV and its phonon side bands G_1 and G_2 are believed to originate from dislocations and extended defects. The ratio of the intensities of the G band to the strongest nitrogen-bound exciton line may be used as a figure of merit for crystalline perfection in CVD 3C-SiC films. It has been found that the biaxial stress in the SiC/Si system depresses the intensity of the non-phonon line as well as the TA, LA, and LO phonon transitions in the nitrogen-bound exciton spectrum.

Single crystal 3C-SiC epitaxial films have been synthesized on Si(1 1 1) using tetramethylsilane by rapid thermal CVD [116]. To prepare free standing films of SiC, the Si substrates are etched using a $HF:HNO_3$ (1:1) solution. The PL spectra of the front surfaces of the SiC/Si samples as well as the back surfaces of the free standing SiC films after removal of the Si substrate have been obtained. The SiC/Si film does not display any luminescence at room temperature [Fig. 36(a)]. In contrast, strong PL centered at about 2.4 eV appears from the free standing SiC films [Fig. 36(b)]. The full widths at half maximum are between 450 and 500 meV, depending on the growth conditions, excitation wavelength, and excitation light intensity. There is an additional weak peak at 3.0 eV. The low temperature (5 K) PL spectrum obtained from the free standing SiC film shows a strong but broad peak similar to that at room temperature. The intensity and peak energy increase with temperature until they reach the maximum values at around 70 K and then decrease at higher temperature. The SEM micrographs show a number of prominent triangular features with dimensions of about 1 μm on the SiC side of the interface. The IR spectra of the free standing SiC films reveal vibration peaks pertaining to the CH and OH groups. Therefore, the origin of the PL appears to be associated with an OH group adsorbed on defects or some localized states similar to that in an amorphous Si_xC_{1-x} alloy.

Intense room temperature PL has been observed from both SiC thin films produced on Si substrates by hot-filament CVD and porous SiC thin films formed by electrochemical

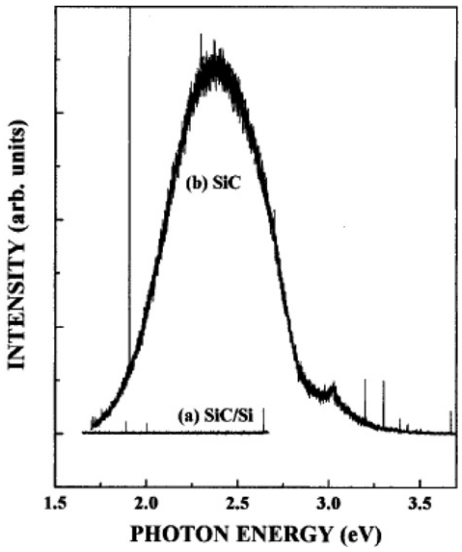

Fig. 36. Room-temperature PL spectra of: (a) SiC/Si, and (b) free standing SiC films excited by the 325 nm line of a He–Cd laser [116].

anodization of SiC thin films in HF–ethanol [117]. SiH_4 and CH_4 diluted with H_2 are used as the precursors in the CVD process. Fig. 37 shows a series of room temperature PL spectra acquired from the anodized SiC sample during continuous irradiation by a He–Cd laser for a duration time of up to 190 min. The initial spectrum shows a strong peak at 1.9 eV, which gradually weakens with increasing irradiation time. In contrast, a new PL peak appears after UV irradiation. Its intensity is greatly enhanced, and the peak shifts from 2.5 to 2.1 eV with longer irradiation time. It should be noted that the peak energy of the new UV irradiation-induced luminescent band from the anodized SiC samples lies in the same energy range as that of the as-grown SiC thin films. Moreover, both spectra are enhanced by continuous UV irradiation. Therefore, they perhaps have the same origins, possibly induced by defect states in SiC which can be activated by UV irradiation.

Films containing nanocrystalline 3C-SiC embedded in an amorphous SiC matrix have been fabricated by hot-filament CVD employing methane and silane as the precursors

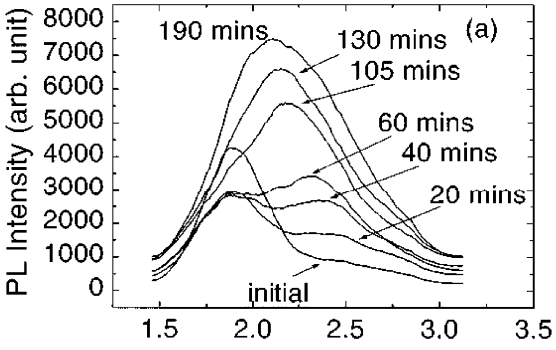

Fig. 37. A series of PL spectra acquired at room temperature under continuous UV irradiation for different periods of time from an anodized SiC thin film prepared by using a current density of 10 mA/cm^2 for 5 min [117].

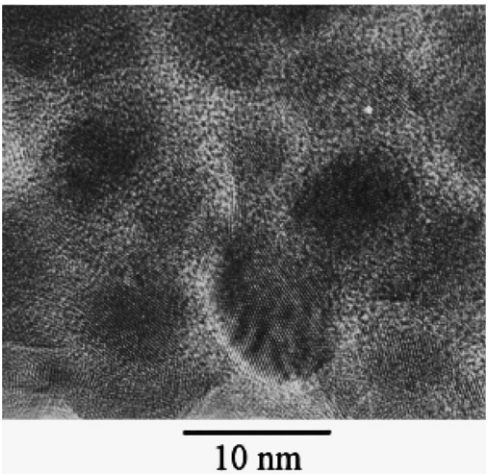

Fig. 38. High resolution TEM image of nanocrystalline 3C-SiC embedded in an amorphous SiC matrix showing the presence of nanocrystallites in the sample [118].

[118]. The HRTEM images show that these films contain embedded nanocrystallites with an average dimension of about 7 nm (Fig. 38). X-ray photoelectron spectroscopy, X-ray diffraction, infrared absorption, and Raman scattering studies reveal that these are 3C-SiC particles. The films display strong visible emission at 2.2 eV that appears to stem from the nanocrystalline 3C-SiC. Hydrogenated nanocrystalline silicon carbide films have also been produced using a similar method [119]. The films which contain SiC nanocrystals embedded in a-SiC:H matrix produce a strong emission peak at 2.64 eV.

Time-resolved PL spectra have been acquired from SiC nanocrystalline films deposited on Si using electron cyclotron resonance (ECR) CVD [120]. Root-temperature optical absorption measurements show a clear blueshift of the band gap with decreasing nanocluster size, as expected from the quantum confinement effect. However, the emission spectra with peak at about 2.4 eV are basically independent of the size. The temporal evolution of the dominant emission suggests double-exponential decay processes (Fig. 39). Two distinct decay times determined to be $\sim$200 ps and $\sim$1 ns are at least two orders of magnitude shorter than that of the bound-exciton transitions in bulk 3C-SiC at low temperature. Based on the intense emission and short decay times, it is speculated that the radiative recombination may arise from some direct transitions such as self-trapped excitons on the surface of the SiC nanocrystals.

Nanocrystalline SiC thin films have been deposited by plasma enhanced CVD at temperatures ranging from 80 to 575 °C using different gas flow ratios [121]. Diethylsilane is used as the source of hydrogen, and argon and helium are used as the dilution gases. The FTIR spectra indicate the formation of SiC nanocrystals embedded in the amorphous matrix at 300 °C. HRTEM confirms the existence of nanocrystallites with sizes ranging from 2 to 10 nm and TEM shows that the film consists of predominantly 3C-SiC with traces of the 4H and 6H polytypes.

Nanocrystalline 4H-SiC films have also been fabricated by plasma enhanced CVD using a mixture of SiH_4, CH_4, and H_2 precursors [122]. The Raman spectra and electron diffraction (ED) patterns indicate that the as-grown films consist of an amorphous

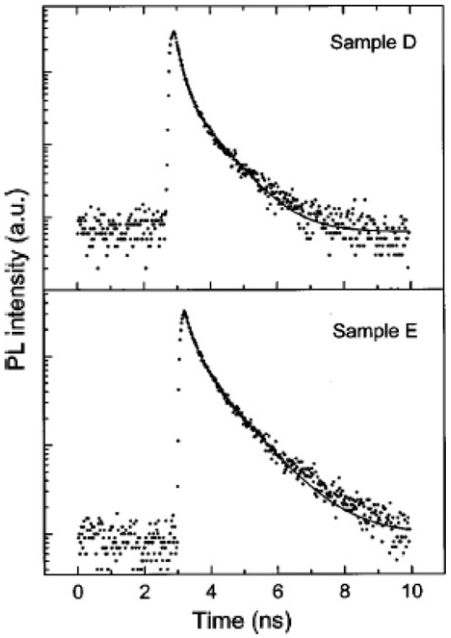

Fig. 39. Room-temperature PL decay curves of the dominant emission peaks of two samples, D and E, fabricated using flow ratios of H_2:SiH_4:CH_4 of 100:10:3 and 100:5:1, respectively. The solid circles represent the experimental data while the solid lines show the biexponential fitted results [120].

network and single-phase crystalline 4H-SiC. The microcolumnar 4H-SiC nanocrystallites with a diameter of about 16 nm are encapsulated in the amorphous SiC network. The films display emission with a peak wavelength of 810 nm when excited by the 514.5 nm line of the Ar^+ laser, and it is conjectured to be related to surface states or defects in the 4H-SiC nanocrystallites.

Blue–green and UV PL have been acquired from 3C-SiC layers synthesized on porous silicon by high temperature pyrolysis of polyimide Langmuir–Blodgett films in vacuum. The PL still exists after thermal treatment at 900 °C [97]. The 4H-SiC nanocrystalline films prepared by a similar method have also been reported [123]. The materials show emission bands centered at ~3.75 eV. Hydrogenated amorphous SiC thin films deposited at a low substrate temperature (100 °C) are found to exhibit red and blue–green PL [124]. Nonstoichiometric and highly disordered SiC films prepared by CVD exhibit PL composed of a series of overlapping bands from 1.8 to 3.3 eV [125].

8. SiC nanowires and nanotubes

8.1. Synthesis using carbon nanotubes

It has been demonstrated that SiO vapor can be used to convert carbon fibers [126] and nanotubes [127] to SiC rods. The size of these SiC products is typically much larger than the carbon precursor. Silicon carbide nanorods with diameters (2–20 nm) similar to that of the starting nanotube reactants and significantly smaller than those previously reported,

however, have been synthesized by reacting carbon nanotubes with SiO or Si–I_2 at about 1200 °C [39]. The lengths of the nanorods are $\leqslant$20 μm. A mechanism encompassing template-mediated growth may explain the formation of the SiC nanorods. The carbon nanotubes define the diameter of the SiC nanorods, but contributions from catalytic growth and/or sintering of the small tubes cannot be ruled out.

Heterostructures of single-walled SiC nanotubes and nanorods have been reported [128]. The method is based on a direct solid–solid reaction: C (nanotubes) + Si (solid) → SiC (solid). The reaction is spatially restricted by partial contact between the surface of the solid Si and carbon nanotubes. The reaction occurs in ultra-high vacuum or in inert gas ambience to get rid of volatile reactants. The silicon carbide initially forms at the C/Si interface at a sufficiently high temperature (generally $T > 800$ °C). Most SWCNT bundles are joined to the crystalline SiC nanorods. The SWCNT/SiC interfaces appear well ordered and do not show an amorphous phase. These nearly ideal heterostructures represent a new kind of nanometer-sized molecular/crystal interface.

A two-step reaction has been developed to synthesize SiC nanorods at 1400 °C [129]. SiO vapor is first generated via reduction of silica, and then the SiO vapor reacts with the carbon nanotubes to form SiC nanorods. The reactions are as follows:

$$SiO_2(s) + Si(s) \rightarrow 2SiO(v) \quad (8)$$

$$SiO(v) + 2C(s) \rightarrow SiC(s) + CO(v) \quad (9)$$

The XRD and Raman spectra show that the SiC has predominantly the β-phase. The TEM images reveal that the diameters of the SiC nanorods range from 3 to 40 nm. The thinner SiC nanorods with diameters of 3 nm show a high density of defect planes. The room temperature PL spectrum of the SiC nanoroads shows a peak at 430 nm (Fig. 40).

The synthesis method described above is very promising since the stable carbon nanotubes serve as the templates that can limit the reaction spatially to the nanotubes, resulting in the formation of nanorods with diameters and lengths similar to those of the carbon nanotubes. Based on a similar method, oriented SiC nanowires have been synthesized by reacting aligned carbon nanotubes with SiO [130]. The high-resolution TEM micrograph in Fig. 41 indicates that the products consist of highly oriented nanowires that resemble the original aligned carbon nanotubes. The SiC nanowires in the arrays have

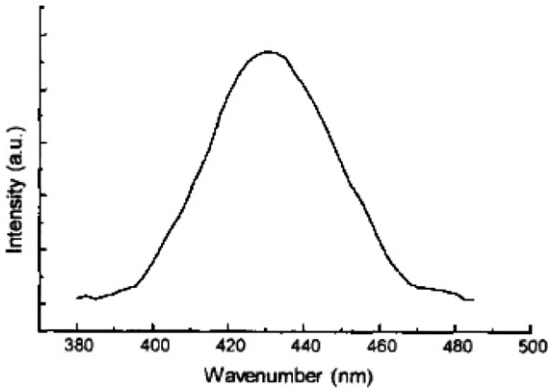

Fig. 40. PL spectrum of SiC nanorods excited by 260 nm fluorescent light [129].

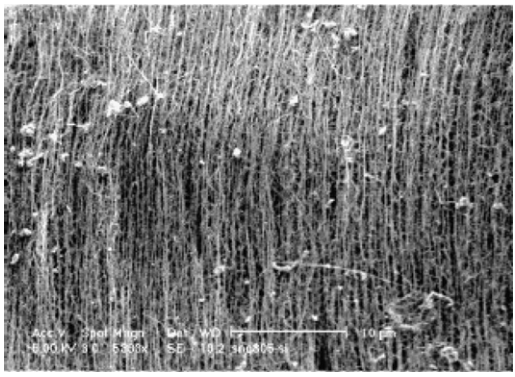

Fig. 41. High-magnification SEM image of a SiC nanowire array showing that the wires are highly aligned and have uniform diameters and spacings among wires. The particles present on the array surface are silicon-containing particles formed during the reaction [130].

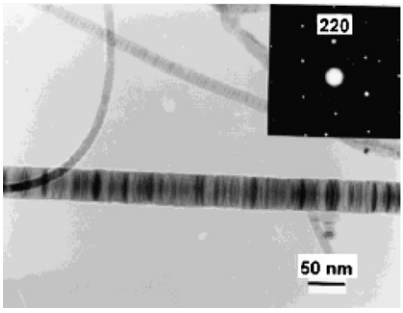

Fig. 42. TEM image of β-SiC nanowires. The SiC nanowires have a high density of stacking faults perpendicular to the wire axes. The inset shows a selected area electron diffraction pattern of the β-SiC nanowires [130].

similar diameters (10–40 nm), spacings (~100 nm), and lengths (up to 2 mm). Fig. 42 shows that instead of the tubular structures that comprise the multilayer carbon nanotubes, the SiC nanowire does not have a hollow core and is a solid rod. The outside of the SiC nanowire is also free of any coated amorphous materials. The SiC nanowire possesses a high density of planar defects and stacking faults which are perpendicular to the wire axes. The selected area electron diffraction (SAED) pattern (inset in Fig. 42) demonstrates that the SiC nanowire has a highly crystalline phase. Field emission examinations show that these oriented SiC nanowires are excellent field emitters possessing large field emission current densities at very low electric fields (2.5–3.5 V/μm).

Silicon carbide nanotubes can also be formed by decomposing SiO on multiwalled carbon nanotubes (MWCNTs) which have been grown on a silicon chip with an aligned orientation at 1250 °C [40]. A typical image of the produced SiC nanotube is shown in Fig. 43. The interlayer spacing of the multiwalled silicon carbide nanotubes is between 3.5 and 4.5 Å.

SiC nanofibers have been synthesized by depositing silicon on the surface of carbon nanotubes followed by annealing at 1200 °C for 15 min using a DC self-heating method [131]. The SiC phase (SiC nanofibers) and graphite phase (carbon nanotubes) coexist in

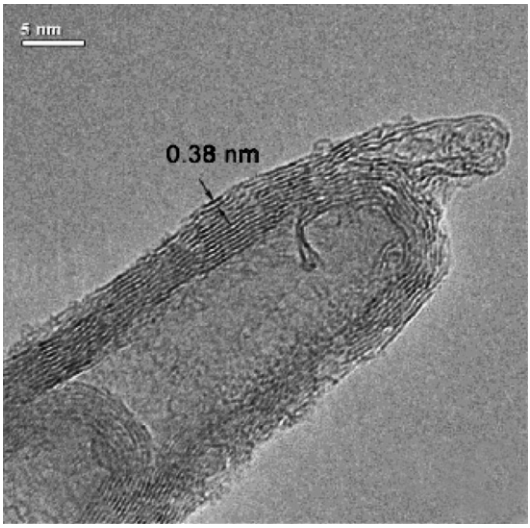

Fig. 43. HRTEM image of an SiC nanotube structure with a spacing of 3.8 Å [40].

the products. Single-phase silicon carbide nanotubes have been successfully synthesized by the reaction between carbon nanotubes and silicon powders at 1200 °C for 100 h [132]. TEM indicates the existence of both the single-phase SiC nanotubes and C-SiC coaxial nanotubes, i.e., carbon nanotubes covered by a SiC layer. The synthesis of carbon-filled silicon carbide nanotubes with a narrow diameter distribution (45–70 nm) has been carried out by reacting multiwalled carbon nanotubes with silicon powders [133].

8.2. Chemical vapor deposition method

β-SiC nanorods can be synthesized on silicon using a solid carbon and silicon source in hot filament CVD [134]. Equal molar amounts of Si and graphite powders are pressed at 150 °C at a pressure of 3.2×10^8 Pa for 24 h to produce a solid plate. It is placed 3 mm above the filament and the silicon (1 0 0) wafer is placed 2 mm below the filament. The filament temperature is 2200 °C. Hydrogen introduced into the reaction chamber etches the solid source and brings reactive Si/C species to the surface of the substrate heated to 1000 °C. After 2 h, a grayish film is obtained and TEM reveals that the film consists of β-SiC nanorods (Fig. 44). Each individual nanorod has a core–shell structure 10–30 nm in diameter. High-resolution TEM demonstrates that the thinner inside core has a crystalline plane, whereas the outer shell has an amorphous phase. Metallic particles of Fe, Ni, and Cr are found on the tips of most of the nanorods, and they are believed to be impurities from the Si powders. The SiC nanorods are produced probably by the vapor–liquid–solid (VLS) growth mechanism [135]. The field emission properties have been studied [136] and Fig. 45 shows the current–voltage (I–V) characteristics of the SiC nanowire film at anode-sample distances from 20 to 120 μm. The I–V curves are relatively smooth and consistent. The turn-on field at which the current density is 0.01 mA/cm^2 is estimated to be ~20 V/μm from the exponentially fitted curves. This turn-on field value is comparable to those of other field emitters such as diamond films and carbon nanotubes.

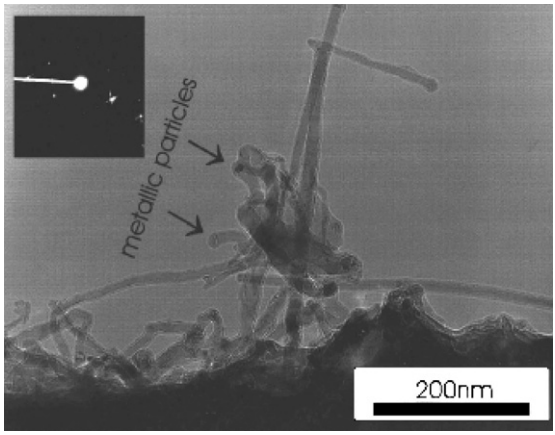

Fig. 44. TEM micrograph of β-SiC nanorods showing the general structure and the corresponding SAD pattern (inset) [134].

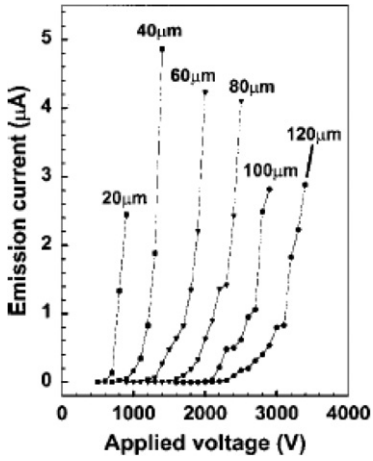

Fig. 45. *I–V* characteristics of a SiC nanowire film at different anode–sample distances [136].

β-SiC nanorods with diameters of 5–20 nm and lengths of about 1 μm have been grown on porous silicon substrates by CVD using iron as the catalyst [137]. A tablet composed of pressed Si and SiO_2 powders is placed in the chamber in which the reaction takes place in the presence of CH_4 and H_2. β-SiC nanorods can also be synthesized by using a solid mixture of graphite, silicon, and silicon dioxide [138]. Silicon carbide nanowires with diameters of 20–50 nm and lengths of several micrometers have been fabricated on Ni (with a thickness of 2 nm) deposited silicon substrates by CVD [139]. Methyltrichlorosilane (CH_3SiCl_3) is the precursor because it has an equal ratio of Si to C and can decompose at a low temperature. X-ray diffraction, HRTEM, and SAED analyses indicate that the nanowires have a single crystalline cubic zinc blend structure with the ⟨1 1 1⟩ orientation. Fig. 46 depicts the nanowires synthesized at a reactor pressure of about 5 Torr for 2 h. Ni

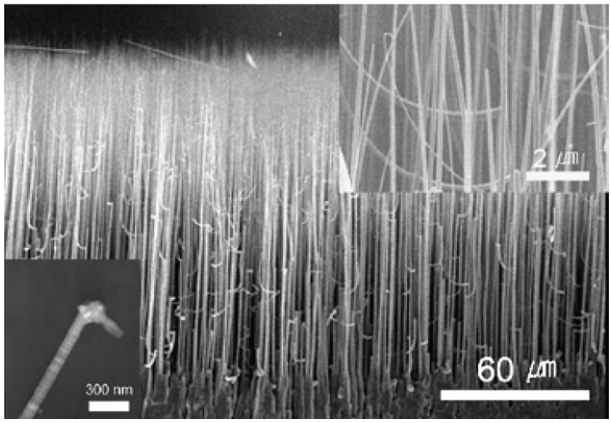

Fig. 46. SEM images of vertically aligned SiC nanowires grown on a Si substrate at 1100 °C for 2 h at a pressure of 5 Torr. The total hydrogen flow rate including carrier and dilute gases is maintained at 775 cm^3 min^{-1}. The lower left inset is a TEM image of a SiC nanowire [139].

alloy is found at the end of the nanowires, suggesting that the VLS mechanism is predominant in the growth of these nanowires.

β-SiC/SiO_2 core/shell nanorods can be synthesized by conducting low temperature (1650 °C) carbothermal reduction and high temperature (1800 °C) heating of sol–gel derived silica xerogels containing carbon nanoparticles [140]. In addition, aligned crystalline silicon carbide nanowires with diameters of about 40 nm can be synthesized directly on silicon via a catalytic reaction at 1100 °C using a methane–hydrogen mixture [141]. SiC nanorods with a typical diameter of about 20 nm have been fabricated on silicon by rapid thermal processing of thin films containing a mixture of carbon and iron at 1000–1200 °C [142]. Single-crystal 3C-SiC nanowhiskers have also been synthesized using microwave plasma CVD [143]. The nanowhiskers exhibit PL in the range of 500–600 nm depending on the synthesis temperature.

Amorphous silicon carbide nanosprings (Fig. 47) as well as biphase (crystalline core/amorphous sheath) helical nanowires have recently been synthesized by plasma enhanced

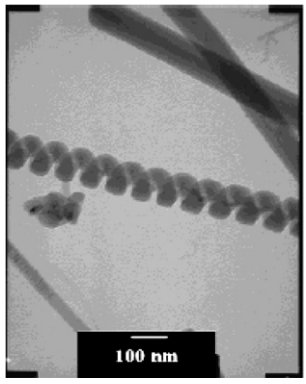

Fig. 47. Bright-field TEM image of an amorphous silicon carbide nanospring [144].

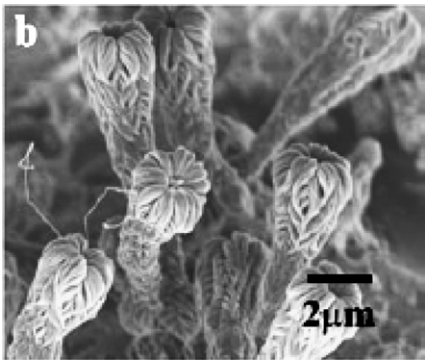

Fig. 48. Plan view SEM image of nanowire flowers grown on silicon [146].

CVD [144]. Here, the $C_2B_{10}H_{12}$ precursor reacts with the Si substrate to form two kinds of structures. The presence of the catalyst at the end of the nanostructures indicates that they are formed by the VLS growth mechanism. The formation of the amorphous silicon carbide nanosprings can be explained by the contact angle anisotropy model [145] previously proposed to explain the formation of amorphous boron carbide nanosprings. A modified contact angle anisotropy model which imposes the presence of temperature gradients within the catalyst has been proposed to explain the formation of the biphase helical nanowires.

Some uncommon SiC nanostructures including three-dimensional crystalline nanowire-based, flower-like structures have been produced by CVD [146]. The silicon substrate and gallium nitride powder are placed in an alumina boat in a tube furnace, and growth of the nanostructures is initiated by the introduction of methane gas at 1100 °C. Fig. 48 depicts the SEM image of the flower-like structures. A typical flower is composed of an intertwined/weaved stem, a bulbous head consisting of a tight bundle of nanowires with diameters of ~100–200 nm, and a single catalyst particle on top of the nanowire flower. The cross-section of the base reveals a hollow stem with a diameter of ~400–800 nm. The flowers are composed of β-SiC and the growth is again governed by the VLS process.

8.3. Direct chemical reaction and other methods

Although reactions based on carbon nanotubes and CVD are the two major methods to synthesize SiC nanowires and nanotubes, some other methods such as direct chemical reactions have been developed. β-SiC nanorods are synthesized by a single-step reaction at 400 °C in a pressurized autoclave with $SiCl_4$ and CCl_4 as the reactants and metallic Na as coreductant [147]. The reaction proceeds as follows:

$$SiCl_4 + CCl_4 + 8Na \rightarrow SiC + 8NaCl \quad (10)$$

The X-ray diffraction pattern indicates the formation of β-SiC. TEM reveals that the product consists of β-SiC nanorods with diameters ranging from 10 to 40 nm and lengths up to several micrometers.

β-phase silicon carbide hollow nanospheres, nanowires, and coaxial nanowires have been reported [148]. Appropriate amounts of $SiCl_4$, C_6Cl_6, and Na are reacted in a stainless steel autoclave at 600 °C for 5–12 h. The SiC hollow nanospheres are generally

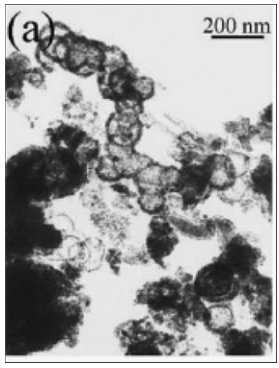

Fig. 49. TEM image of SiC hollow nanospheres [148].

50–100 nm in diameter and 10 nm in thickness (Fig. 49). The SiC nanowires typically have diameters of 20 nm and lengths up to 10 μm. Liquid globules are found on the tip of the nanowires as shown in the TEM micrograph, again suggesting that the VLS mechanism is dominant.

3C-SiC nanowires with diameters of 15–20 nm and lengths of 5–10 μm can be synthesized at 700 °C by a reduction–carburization method [149]. Silicon powders and tetrachloride (CCl_4) are used as the reactants and metallic Na is the reductant. The nanowires exhibit a PL peak at 448 nm. The liquid globules appear on the tip of the nanowires suggest the VLS mechanism.

β-SiC nanowires can be synthesized from a mixture of activated carbon and sol-gel derived silica embedded with Fe nanoparticles [150]. Fig. 50(a) shows that the product is composed of wire-like structures 20–50 nm in diameter and several tens of micrometers in length. X-ray diffraction and TEM show that the nanowires consist of a single crystalline core of β-SiC enclosed by an amorphous layer of silicon oxide [Fig. 50(b)]. The formation process involves carbothermal reduction and proceeds with a VLS growth mechanism. Two PL peaks at about 340 and 440 nm have been observed from the nanowires.

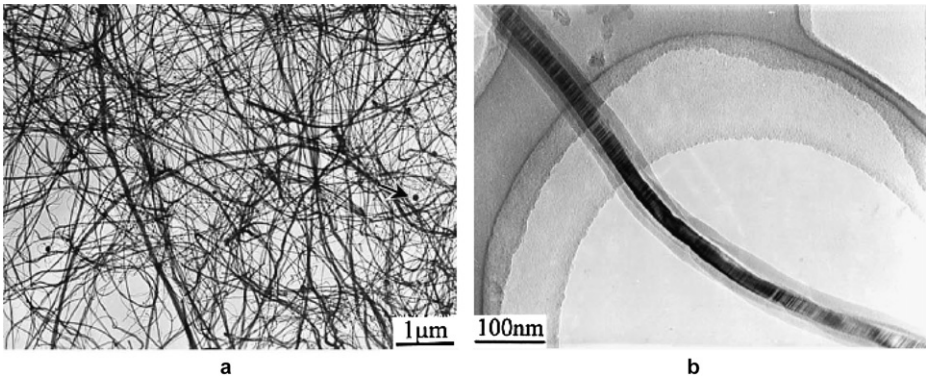

Fig. 50. (a) Low-magnification TEM image showing large quantities of nanowires. (b) A high-magnification TEM image of an individual nanowire [150].

Nanometer-sized SiC whiskers have been synthesized by the arc discharge process [151]. The samples are prepared by triggering an arc discharge between the two graphite electrodes. The anode is composed of a mixture of silicon and graphite powders. The process produces two types of nanostructures: nanosized equiaxed particles with diameters of 10–20 nm, and rod-like structures with diameters of about 10 nm and lengths of more than 100 nm. The rod-like structures are found only when iron is used as a catalyst in the arc discharge process. Fig. 51 shows the HRTEM micrographs of two rod-like nanostructures with lattice fringes parallel and perpendicular to the rod axis. The nanorods are enclosed by an amorphous graphite layer. Only nanorods with a fringe orientation perpendicular or parallel to the rod axis can be found and no measurable amounts of iron are found on the SiC whiskers. Therefore, a two stage VLS growth mechanism in which the Fe catalyst is evaporated in the second step has been proposed.

Cone-shaped hexagonal 6H-SiC nanorods with diameters of 10–30 nm have been produced using the arc discharge process [152]. Formation of the gradually enlarged Fe–Al–Si–C droplets and their high enthalpy lead to the growth of the nanostructures via a VLS mechanism. Silicon carbide nanowires with diameters of 59–110 nm have also been synthesized by laser ablation of a SiC target [153]. The growth of the nanowires can again be explained based on the VLS mechanism. The red shift, broadened peak, and asymmetry

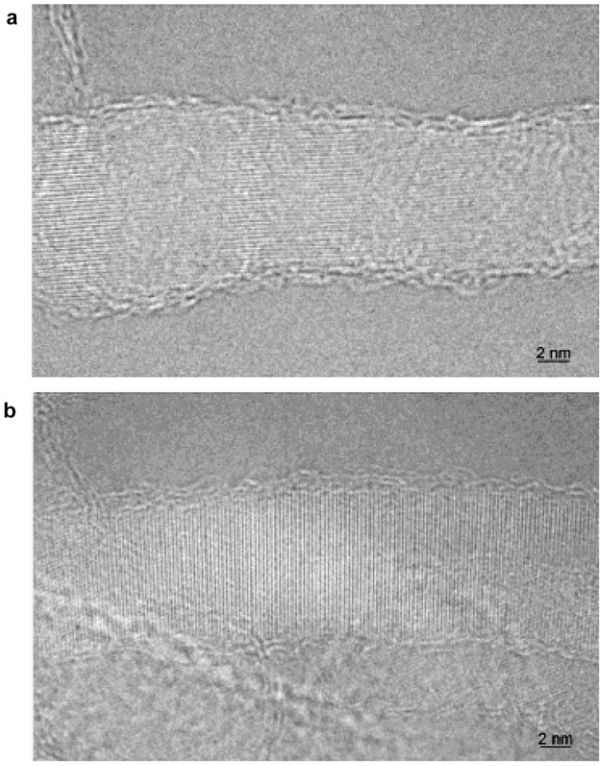

Fig. 51. HRTEM micrographs of two nanowhiskers with the lattice fringes of the whisker are oriented being (a) parallel or (b) perpendicular to its axis. The fringe spacing is 0.243 ± 0.010 nm. The whisker is surrounded by disordered graphite [151].

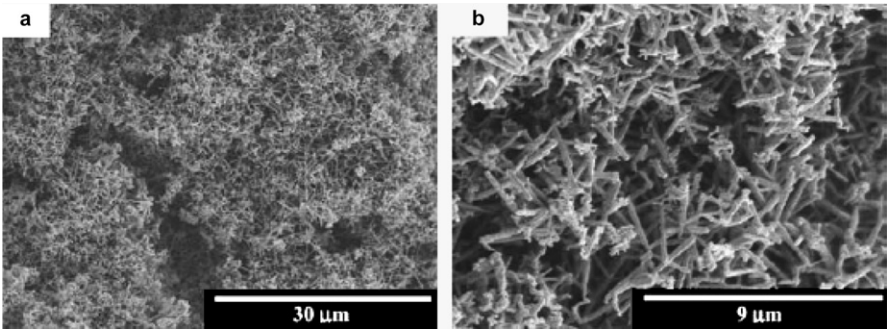

Fig. 52. (a) SEM micrograph of the SiC nanorods synthesized at 1700 °C for 2 h. (b) High magnification SEM micrograph showing that the nanorods are the only pyrolysis products [154].

observed in the Raman spectra can be accounted for by the size confinement effect in the radial and growth directions.

The synthesis of β-SiC nanorods by pyrolysis of a polysilazane polymeric precursor in the presence of 3 wt% $FeCl_2$ as a catalyst has been reported [154]. Fig. 52(a) shows a SEM picture of the SiC nanorods. High magnification SEM indicates that the pyrolysis products contain only nanorods [Fig. 52(b)] which are 80–200 nm in diameter and 4 μm in length. The SAED pattern reveals that the nanorods are oriented along the [1 1 1] direction. A solid–liquid–solid (SLS) growth mechanism is proposed.

Three other methods have been employed to synthesize β-SiC nanowires [155]. In this first procedure, silica gel mixed with activated carbon is dried and heated to 1360 °C for 4–7 h in a NH_3 or H_2 atmosphere. The second one is a solid state synthesis method in which silica is mixed with activated carbon. The mixture is subsequently reduced under conditions similar to those in the first process. In the third method, the gel formed by ethylene glycol, citric acid, and tetraethylorthosilicate (TEOS) is heated in a reducing atmosphere at 1360 °C. All three processes yield wool-like products with β-SiC nanowires as the major component. They are generally several hundreds of nanometers in diameter and have lengths of several tens of micrometers. Fig. 53 shows a PL spectrum acquired from the β-SiC nanowires synthesized by the first procedure showing a peak at about 400 nm.

Cubic silicon carbide nanowires with a needle shape can be grown in bunches by thermal evaporation of SiC powders with iron as the catalyst [156,157]. Fig. 54 shows the SEM micrograph of the SiC nanowires. Individual nanowires evolve from the particles and as a result, each individual particle ''holds'' a bunch of nanowires. The nanowires have diameters between 20 and 50 nm and lengths from 1 to 2 μm. HRTEM images show that the nanowires are crystalline with an atomic spacing of about 4.54 Å which is close to the value of bulk 3C-SiC [158]. The growth direction is [1 0 0]. Fig. 55 discloses the relationship between the emission current and electric field for the typical SiC nanowires. The electron emission turn-on field and threshold field, defined as the macroscopic fields required to produce a current density of 10 $\mu A/cm^2$ and 10 mA/cm^2, respectively, are about 5 and 8.5 V/μm. These values are similar to those of carbon nanotubes [159,160]. The emission behavior can be attributed to the needle-shaped emitting surfaces. The linearity in the Fowler–Nordheim curve indicates that the conventional field emission mechanism is dominant. The growth of the nanowires is surmised to follow the VSL mechanism. A broad PL peak at 450 nm is observed from the nanowires at room temperature [157].

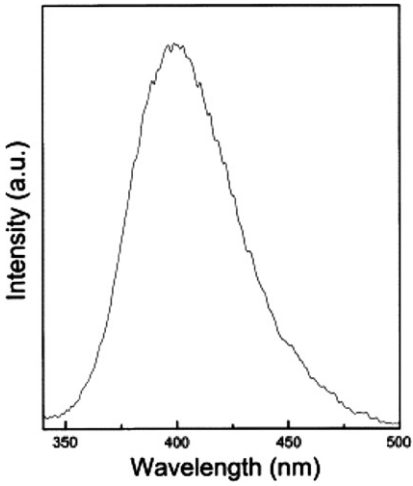

Fig. 53. PL spectrum of SiC nanowires synthesized by procedure (i) (heating the gel containing activated carbon and silica for 7 h at 1360 °C in NH_3) [155].

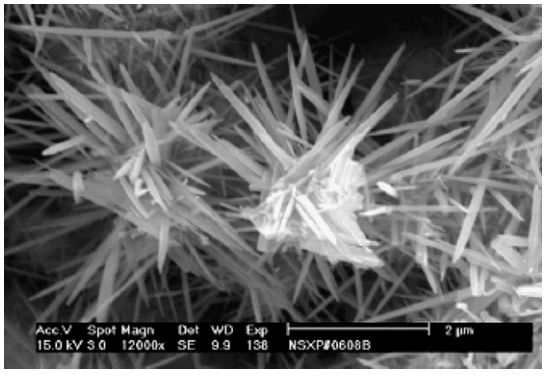

Fig. 54. SEM micrograph of SiC nanowire bunches [157].

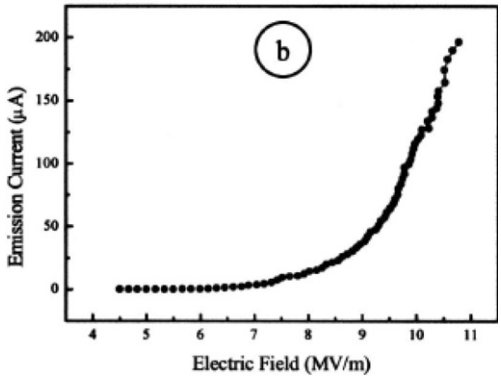

Fig. 55. Field electron emission direct current–voltage characteristics of SiC nanowires [156].

8.4. Miscellaneous notes

Generally, the SiC nanowires produced by the aforementioned methods have diameters of several tens of nanometers and lengths varying from several to tens of micrometers. However, SiC nanowires as small as several nanometers [39,137,143] or as large as several hundreds of nanometers [154,155] in diameter have been synthesized. In most cases, the produced nanostructures are in the forms of nanowires or nanorods. Nanotubes [40,128,132,133] have been prepared in some experiments. Some less common structures such as nanospheres [148], nanosprings [144], and nanowire flowers [146] have also been observed. Almost all the synthesized one-dimensional silicon carbide nanostructures have the cubic zinc blende structure (β-SiC), although a few hexagonal structures have also been discovered [142].

There have been several reports on the PL of SiC nanowires. The PL spectra are generally smooth showing a single emission peak between 400 and 450 nm [129] that is above the bulk band gap of 3C-SiC. Some nanowires have been found to exhibit PL with a peak between 500 and 600 nm [143]. The luminescence mechanism is not well known.

Compared to the photoluminescence of one-dimensional SiC nanocrystals, even less is known about their electronic structures. One recent investigation [38] makes use of preliminary density-functional calculation of the geometrical and electronic structures of silicon carbide nanowires. The supercells of 57 and 114 atoms of the surface reconstructed SiC nanowires and 93 atoms of the hydrogen passivated SiC nanowires are studied. It is found that the SiC nanowires have a wider band gap compared to bulk crystalline SiC due to quantum confinement. With regard to the pure nanowires, the facets' dangling bonds reconstruct substantially and the surface turns into a metallic state.

9. Summary

As silicon-based microelectronic devices are approaching the physical limits, the constant push to develop better and faster devices and higher computing power has spurred the development of substituting materials. In this regard, silicon carbide is a good candidate in high-power, high-temperature, and high-frequency applications. The optical and electrical properties of nanometer-sized silicon carbide structures are particularly crucial to efficient and stable SiC nanodevices. SiC nanowires have been shown to have stable field electron emission properties [130,156], suggesting that the materials have potential as field electron emitters. The heterostructures of single-walled carbon nanotubes and silicon carbide nanorods [128] may play an important role in future hybrid nanodevices. The intense, robust and wavelength-tunable visible emission from 3C-SiC nanocrystals shows that they are good light sources [33] applicable to nano-optoelectronic integration. Nanocrystalline SiC films which emit visible light [119] are also promising in large area displays. Furthermore, silicon carbide is a biocompatible material [161] and biosensors made of these materials may be realized in the future. Considering the chemical stability and water-solubility, luminescent silicon carbide nanocrystals may find applications in biotechnology/medicine [35].

Extensive studies of silicon carbide nanostructures such as nanocrystals, nanowires and nanotubes, and nanosized films began in the mid-1990s and we aim at reviewing the important results published in the past 10 years in this paper. However, it should be noted that researches on silicon carbide nanostructures are still in the beginning stage. Although

clear quantum confinement of 3C-SiC has been observed [33], the specific defect or surface states responsible for the observed luminescence have not been unequivocally identified. Much more experimental and theoretical work is needed. In addition, although large quantities of SiC nanowires, including oriented SiC nanowires [130], can now be produced, reports on their physical properties and related device designs are relatively few, and little is known about the properties of nanocrystalline SiC films. Finally, there have only been a few theoretical studies on SiC nanostructures. A better understanding of the various properties of these nanostructures is needed in order to realize their full potentials.

Acknowledgement

This work was jointly supported by Grants Nos. 10225416, 60476038, and 60576061 from the Natural Science Foundations of China, the LPEMST, the special funds for Major state Basic Research Project (No. G2001CB3095) of China, Hong Kong Research Grants Council (RGC) Competitive Earmarked Research Grant (CERG) No. CityU 1120/04E, and City University of Hong Kong Direct Allocation Grant No. 9360110.

References

[1] Harris CI, Savage S, Konstantinov A, Bakowski M, Ericsson P. Appl Surf Sci 2001;184:393.
[2] Masri P. Surf Sci Rep 2002;48:1.
[3] Nakamura D, Gunjishima I, Yamaguchi S, Ito T, Okamoto A, Kondo H, et al. Nature 2004;430:1009.
[4] Devaty RP, Choyke WJ. Phys Stat Sol (a) 1997;162:5.
[5] Canham LT. Appl Phys Lett 1990;57:1046.
[6] Cullis AG, Canham LT, Calcott DJ. J Appl Phys 1997;82:1.
[7] Brus LE, Szajowski PF, Wilson WL, Harris TD, Schupler S, Citrin PH. J Am Chem Soc 1995;117:2915.
[8] Efros AlL, Efros AL. Sov Phys Semicond 1982;16:772.
[9] Brus L. J Chem Phys 1983;79:5566.
[10] Morkoc H, Strite S, Gao GB, Lin ME, Sverdlov B, Burns M. J Appl Phys 1994;76:1363.
[11] Carter GE, Casady JB, Bonds J, Okhuysen ME, Scofield JD, Saddow SE. Mater Sci Forum 2000;338–342:1149.
[12] Madelung O. Semiconductors: Data handbook. 3rd ed. Berlin: Springer; 2004.
[13] Chan WCW, Nie S. Science 1998;281:2016.
[14] Bruchez Jr M, Moronne M, Gin P, Weiss S, Alivisatos AP. Science 1998;281:2013.
[15] Matsumoto T, Takahashi J, Tamaki T, Futagi T, Mimura H, Kanemitsu Y. Appl Phys Lett 1994;64:226.
[16] Shor JS, Bemis L, Kurtz AD, Grimberg I, Weiss BZ, MacMillian MF, et al. J Appl Phys 1994;76:4045.
[17] Petrova-Koch V, Sreseli O, Polisski G, Kovalev D, Muschik T, Koch F. Thin Solid Films 1995;255:107.
[18] Konstantinov AO, Henry A, Harris CI, Janzén E. Appl Phys Lett 1995;66:2250.
[19] Liao LS, Bao XM, Yang ZF, Min NB. Appl Phys Lett 1995;66:2382.
[20] Shor JS, Zhang XG, Osgood RM. J Electrochem Soc 1992;139:1213.
[21] Takazawa A, Tamura T, Yamada M. Jpn J Appl Phys 1993;32:3148.
[22] Zhao J, Mao DS, Lin ZX, Jiang BY, Yu YH, Liu XH, et al. Appl Phys Lett 1998;73:1838.
[23] Wu XL, Siu GG, Stokes MJ, Fan DL, Gu Y, Bao XM. Appl Phys Lett 2000;77:1292.
[24] Lehmann V, Gösele U. Appl Phys Lett 1991;58:856.
[25] Heinrich J, Curtis CL, Credo GM, Kavanagh KL, Sailor MJ. Science 1992;255:66.
[26] Brus LE, Szajowski PF, Wilson WL, Harris TD, Schuppler S, Citrin PH. J Am Chem Soc 1995;117:2915.
[27] Belomoin G, Therrien J, Smith A, Rao S, Twesten R, Chaieb S, et al. Appl Phys Lett 2002;80:841.
[28] Ledoux G, Gong J, Huisken F, Guillois O, Reynaud C. Appl Phys Lett 2002;80:4834.
[29] Starke U. Phys Stat Sol (b) 1997;202:475.
[30] Soukiassian P. Mater Sci Eng B 2002;96:115.
[31] Derycke V, Soukiassian PG, Amy F, Chabal J, D'Angelo MD, Enriquez HB, et al. Nature 2003;2:253.
[32] Brillson LJ, Tumakha S, Okojie RS, Zhang M, Pirouz P. J Phys: Condens Matter 2004;16:S1733.

[33] Wu XL, Fan JY, Qiu T, Yang X, Siu GG, Chu PK. Phys Rev Lett 2005;94:026102.
[34] Feng DH, Xu ZZ, Jia TQ, Li XX, Gong SQ. Phys Rev B 2003;68:035334.
[35] Bailey RE, Smith AM, Nie S. Physica E 2004;25:1.
[36] Fan JY, Wu XL, Kong F, Qiu T, Huang GS. Appl Phys Lett 2005;86:171903.
[37] Reboredo FA, Pizzagalli L, Galli G. Nano Lett 2004;4:801.
[38] Rurali R. Phys Rev B 2005;71:205405.
[39] Dai H, Wong EW, Lu YZ, Fan S, Lieber CM. Nature 1995;375:769.
[40] Sun XH, Li CP, Wong WK, Wong NB, Lee CS, Lee ST, et al. J Am Chem Soc 2002;124:14464.
[41] Appell A. Nature 2002;419:553.
[42] Choyke WJ, Feng ZC, Powell JA. J Appl Phys 1988;64:3163.
[43] Jennings VJ. Mater Res Bull 1969;4:S-199.
[44] Palmour JW, Davis RF, Astell-Burt P, Blackborow P. In: Howard RE, Hu EL, Namba S, Pang SW, editors. Science and technology of microfabrication. Pittsburgh: Material Research Society; 1987. p. 185.
[45] Carraba MM, Li J, Hachey JP, Rauh RD, Wang Y. Electrochem Soc Extended Abstracts 1989;89 (2):727.
[46] Shor JS, Osgood RM, Kurtz AD. Appl Phys Lett 1992;60:1001.
[47] Shor JS, Grimberg I, Weiss BZ, Kurtz AD. Appl Phys Lett 1993;62:2836.
[48] Smith RL, Collins SD. J Appl Phys 1992;71:R1.
[49] Nychyporuk T, Lysenko V, Barbier D. Phys Rev B 2005;71:115402.
[50] Wolfe JP. Phys Today 1982 (March):46.
[51] Konstantinov AO, Harris CI, Janzén. Appl Phys Lett 1994;65:2699.
[52] Shishkin Y, Choyke WJ, Devaty RP. J Appl Phys 2004;96:2311.
[53] Shishkin Y, Ke Y, Devaty RP, Choyke WJ. J Appl Phys 2005;97:044908.
[54] Masuda H, Yamada H, Satoh M, Asoh H, Nakao M, Tamamura T. Appl Phys Lett 1997;71:2770.
[55] Lehmann V, Föll H. J Electrochem Soc 1990;137:653.
[56] Zangooie S, Woollam JA, Arwin H. J Mater Res 2000;15:1860.
[57] Rittenhouse TL, Bohn PW, Adesida I. Solid State Commun 2003;126:245.
[58] Kato M, Ichimura M, Arai E, Ramasamy P. Jpn J Appl Phys 2003;42:4233.
[59] Choyke WJ, Patrick L. Phys Rev B 1970;2:4959.
[60] Ikeda M, Matsunami H, Tanaka T. Phys Rev B 1980;22:2842.
[61] Lockwood DJ, Aers GC, Allard LB, Bryskiewicz B, Charbonneau S, Houghton DC, et al. Can J Phys 1992;70:1184.
[62] Makarov VV. Sov Phys Solid State 1972;13:1774.
[63] Patrick L. Mater Res Bull 1969;4s:129.
[64] Jessensky O, Müller F, Gösele U. Thin Solid Films 1997;297:224.
[65] Canham LT, Cullis AG, Pickering C, Dosser OD, Cox TI, Lynch TP. Nature 1994;368:133.
[66] Hassen F, M'Ghaieth R, Maaref H, Madar R. Mater Sci Eng C 2001;15:113.
[67] Rittenhouse TL, Bohn PW, Hossain TK, Adesida I, Lindesay J, Marcus A. J Appl Phys 2004;95:490.
[68] Parkhuik VP, Namavar F, Andrade E. Thin Solid Films 1997;279:229.
[69] Kim S, Spanier JE, Herman IP. Jpn J Appl Phys 2000;39:5875.
[70] Lee KH, Du YL, Lee TH. Bull Korea Chem Soc 2000;21:769.
[71] Chen ZM, Ma JP, Yu MB, Wang JN, Ge WK, Woo PW. Mater Sci Eng B 2000;75:180.
[72] Xie E, Zhang Z, Ma Z, Lin H, He D. Opt Mater 2003;23:157.
[73] Torchynska TV, Cano AD, Sandoval SJ, Dybic M, Ostapenko S, Mynbaeva M. Microelectron J 2005;36:536.
[74] Danishevskii AM, Zamoryanskaya MV, Sitnikova AA, Shuman VB, Suvorova AA. Semicond Sci Technol 1998;13:1111.
[75] Koch F, Petrova-Koch V, Muschik T. J Lumin 1993;57:271.
[76] Wolkin MV, Jorne J, Fauchet PM. Phys Rev Lett 1999;82:197.
[77] Wu XL, Xiong SJ, Fan DL, Gu Y, Bao XM. Phys Rev B 2000;62:R7759.
[78] Borders JA, Picraux ST, Beezhold W. Appl Phys Lett 1971;18:509.
[79] Zhang Z. Microsc Res Techn 1998;40:163.
[80] Gao YH, Zhang Z, Liao LS, Bao XM. J Mater Res 1997;12:1640.
[81] Li X, Shao C, Qiu S, Xiao FS, Zheng W, Liu Z, et al. Mater Lett 2001;48:242.
[82] Yamamoto M, Hayashi R, Tsunetomo K, Kohno K, Osaka Y. Jpn J Appl Phys 1991;30:136.
[83] Osaka Y, Tsunetomo K, Toyomura F, Myoren H, Kohno K. Jpn J Appl Phys 1992;31:L365.
[84] Weinberg ZA, Rubloff GW, Bassous E. Phys Rev B 1979;19:3107.

[85] Pérez-Rodríguez A, González-Varona O, Garrido B, Pellegrino P, Morante JR, Bonafos C, et al. J Appl Phys 2003;94:254.
[86] Regohle L, Gebel T, Fröb, Reuther H, Skorupa W. Appl Surf Sci 2001;184:156.
[87] Chen D, Liao ZM, Wang L, Wang HZ, Zhao F, Cheung WY, et al. Opt Mater 2003;23:65.
[88] Yu YH, Wong SP, Wilson IH. Phys Stat Sol (a) 1998;168:531.
[89] Guo YP, Zheng JC, Wee ATS, Huan CHA, Li K, Pan JS, et al. Chem Phys Lett 2001;339:319.
[90] An Z, Fu RKY, Chen P, Liu W, Chu PK, Lin C. J Vac Sci Technol B 2003;21:1375.
[91] Hamza AV, Balooch M, Moalem M. Surf Sci 1994;317:L1129.
[92] Chen D, Workman R, Sand D. Surf Sci 1995;344:23.
[93] Henke S, Stritzker B, Rauschenbach B. J Appl Phys 1995;78:2070.
[94] Moro L, Paul A, Lorents DC, Malhotra R, Ruoff RS, Lazzeri P, et al. J Appl Phys 1997;81:6141.
[95] Song HZ, Bao XM, Li NS, Wu XL. Appl Phys Lett 1998;72:356.
[96] Kim K, Suh MS, Kim TS, Youn CJ, Suh EK, Shin YJ, et al. Appl Phys Lett 1996;69:3908.
[97] Liu R, Yang B, Fu Z, He P, Ruan Y. Solid State Commun 1998;106:211.
[98] Rozhin AG, Klyui NI, Litovchenko VG, Piryatinskii YP. Mater Sci Eng C 2002;19:229.
[99] Heera V, Fontaine F, Skorupa W, Pécz B, Barna Á. Appl Phys Lett 2000;77:226.
[100] Weishart H, Eichhorn F, Heera V, Pécz B, Barna Á, Skorupa W. J Appl Phys 2005;98:043503.
[101] Buschmann V, Klein S, Fueß H, Hahn H. J Crystal Growth 1998;193:335.
[102] Kassiba A, Makowska-Janusik M, Bouclé J, Bardeau JF, Bulou A, Herlin-Boime N. Phys Rev B 2002;66:155317.
[103] Cauchetier M, Croix O, Luce M. Adv Ceram Matter 1988;3–6:197.
[104] Bouclé J, Kassiba A, Makowska-Janusik M, Sanetra J, Herlin-Boime N, Bulou A, et al. Opt Commun 2005;246:415.
[105] Yajima S, Hayasht J, Omori M. Chem Lett 1975;931.
[106] Yajima S, Hasegawa Y, Omori M, Okamura K. Nature 1976;261:683.
[107] Wang CH, Chang YH, Yen MY, Peng CW, Lee CY, Chiu HT. Adv Mater 2005;17:419.
[108] Fojtik A, Weller H, Fiechter S, Henglein A. Chem Phys Lett 1987;134:477.
[109] Takagi H, Ogawa H, Yamazaki Y, Ishizaki A, Nakagiri T. Appl Phys Lett 1990;56:2379.
[110] DiMaria DJ, Kirtley JR, Pakulis EJ, Dong DW, Kuan TS, Pesavento FL, et al. J Appl Phys 1984;56:401.
[111] Ito T, Kiyama H, Yasumatsu T, Watabe H, Hiraki A. Physica B 1991;170:535.
[112] Gupta P, Colvin VL, George SM. Phys Rev B 1988;37:8234.
[113] Perdew JP, Burke K, Ernzerhof M. Phys Rev Lett 1996;77:3865.
[114] Williamson A, Grossman J, Hood R, Puzder A, Galli G. Phys Rev Lett 2002;89:196803.
[115] Puzder A, Williamson AJ, Reboredo FA, Galli G. Phys Rev Lett 2003;91:157405.
[116] Shim HW, Kim KC, Seo YH, Nahm KS, Suh EK, Lee HJ, et al. Appl Phys Lett 1997;70:1757.
[117] Wang JN, Chen ZM, Woo PW, Ge WK, Wang YQ. Appl Phys Lett 1999;74:923.
[118] Yu MB, Rusli, Yoon SF, Chen ZM, Ahn J, Zhang Q, et al. J Appl Phys 2000;87:8155.
[119] Yu MB, Rusli, Yoon SF, Xu SJ, Chew K, Cui J, et al. Thin Solid Films 2000;377–378:177.
[120] Xu SJ, Yu MB, Rusli, Yoon SF, Che CM. Appl Phys Lett 2000;76:2550.
[121] Rajagopalan T, Wang X, Lahlouh B, Ramkumar C, Dutta P, Gangopadhyay S. J Appl Phys 2003;94:5252.
[122] Zhang H, Xu Z. Thin Solid Films 2004;446:99.
[123] Fu Z, Yan B, Liu R, Ruan Y. J Mater Res 2002;17:570.
[124] Xu J, Yang L, Rui Y, Mei J, Zhang X, Li W, et al. Solid State Commun 2005;133:565.
[125] Danishevskiĭ AM, Shuman VB, Guk EG, Rogachev AY. Semiconductors 1997;31:354.
[126] Okada K, Nakajima K. Eur Patent Applic 1993;EP 60388 A2.
[127] Zhou D, Seraphin S. Chem Phys Lett 1994;222:233.
[128] Zhang Y, Ichihashi T, Landree E, Nihey F, Iijima S. Science 1999;285:1719.
[129] Han W, Fan S, Li Q, Liang W, Gu B, Yu D. Chem Phys Lett 1997;265:374.
[130] Pan Z, Lai HL, Au FCK, Duan X, Zhou W, Shi W, et al. Adv Mater 2000;12:1186.
[131] Liu JW, Zhong DY, Xie FQ, Sun M, Wang EG, Liu WX. Chem Phys Lett 2001;348:357.
[132] Tahuchi T, Igawa N, Yamamoto H. J Am Ceram Soc 2005;88:459.
[133] Borowiak-Palen E, Ruemmeli MH, Gemming T, Knupfer M, Biedermann K, Leonhardt A, et al. J Appl Phys 2005;97:056102.
[134] Zhou XT, Wang N, Lai HL, Peng HY, Bello I, Wong NB, et al. Appl Phys Lett 1999;74:3942.
[135] Wagner RS, Ellis WC. Appl Phys Lett 1964;4:89.
[136] Wong KW, Zhou XT, Au FCK, Lai HL, Lee CS, Lee ST. Appl Phys Lett 1999;75:2918.

[137] Zhou XT, Lai HL, Peng HY, Au FCK, Liao LS, Wang N, et al. Chem Phys Lett 2000;318:58.
[138] Lai HL, Wong NB, Zhou XT, Peng HY, Au FCK, Wang N, et al. Appl Phys Lett 2000;76:294.
[139] Choi HJ, Seong HK, Lee JC, Sung YM. J Crystal Growth 2004;269:472.
[140] Meng GW, Zhang LD, Mo CM, Zhang SY, Qin Y, Feng SP, et al. Solid State Commun 1998;106:215.
[141] Kim HY, Park J, Yang H. Chem Commun 2003;2:256.
[142] Yang TH, Chen CH, Chatterjee A, Li HY, Lo JT, Wu CT, et al. Chem Phys Lett 2003;379:155.
[143] Zhang Y, Nishitani-Gamo M, Xiao C, Ando T. J Appl Phys 2002;91:6066.
[144] Zhang D, Alkhateeb A, Han H, Mahmood H, Mcllroy DN, Norton MG, et al. Nano Lett 2003;3:983.
[145] McIlroy DN, Zhang D, Kranov Y, Norton MG. Appl Phys Lett 2001;79:1540.
[146] Ho GW, Wong ASW, Kang DJ, Welland ME. Nanotechnology 2004;15:996.
[147] Lu Q, Hu J, Tang K, Qian Y, Zhou G, Liu X, et al. Appl Phys Lett 1999;75:507.
[148] Shen G, Chen D, Tang K, Qian Y, Zhang S. Chem Phys Lett 2003;375:177.
[149] Hu JQ, Lu QY, Tang KB, Deng B, Jiang RR, Qian YT, et al. J Phys Chem B 2000;104:5251.
[150] Liang CH, Meng GW, Zhang LD, Wu YC, Cui Z. Chem Phys Lett 2000;329:323.
[151] Seeger T, Kohler-Redlich P, Rühle M. Adv Mater 2000;12:279.
[152] Li Y, Xie S, Zhou W, Ci L, Bando Y. Chem Phys Lett 2002;356:325.
[153] Shi W, Zheng Y, Peng H, Wang N, Lee CS, Lee ST. J Am Ceram Soc 2000;83:3228.
[154] Yang W, Miao H, Xie Z, Zhang L, An L. Chem Phys Lett 2004;383:441.
[155] Gundiah G, Madhav GV, Govindaraj A, Seikh MM, Rao CNR. J Mater Chem 2002;12:1606.
[156] Wu ZS, Deng SZ, Xu NS, Chen J, Zhou J, Chen J. Appl Phys Lett 2002;80:3829.
[157] Feng DH, Jia TQ, Li XX, Xu ZZ, Chen J, Deng SZ, et al. Solid State Commun 2003;128:295.
[158] Joint Committee on Powder Diffraction Standards (JCPDS) File No. 29-1129, International Center for Diffraction Data, 1982.
[159] De Heer WA, Chatelain A, Ugarte D. Science 1995;270:1179.
[160] Rinzeler AG, Hafner JH, Nikolaev P, Lou L, Kim SG, Tomanek D, et al. Science 1995;269:1550.
[161] Cicero G, Catellani A, Galli G. Phys Rev Lett 2004;93:016102.